# Wintertime Evolution of Landfast Ice Stability in Alaska from InSAR

Andrew ~~H.~~ Einhorn[1,2,3], and Andrew ~~R.~~ Mahoney[1]

[1]Geophysical Institute, University of Alaska Fairbanks, Fairbanks, 99775, United States of America
[2]~~Insitute~~Institute for Marine and Antarctic Studies, University of Tasmania, Hobart, 7001, Australia
[3]Australia Antarctic Program Partnership, Institute for Marine and Antarctic Studies, University of Tasmania, Hobart, 7001, Australia

Correspondence ~~to~~: Andrew Einhorn (andrew.einhorn@utas.edu.au)

Abstract

. Landfast ice in Alaska is experiencing rapid changes in extents and duration, impacting the safety and utility of the ice for Arctic coastal communities. Current datasets of landfast ice only distinguish landfast ice from mobile pack ice, omitting crucial information regarding the relative safety within landfast ice. InSAR (Interferometric Synthetic Aperture Radar) holds promise for identification of landfast ice and measurement of cm-scale deformation from a spaceborne sensor. We use two properties of interferometry: coherence to identify areas of landfast ice, and the interferometric phase gradient to approximate a new metric called apparent strain ~~($\epsilon_a$)~~($\epsilon_a$) which acts as a proxy for estimating the relative stability of the landfast ice. Apparent strain is described as the horizontal gradient of interferometric phase in the line-of-sight displacement. We built on a previous study by Dammann et al. (2019) by assigning quantitative apparent strain values to identify 3 distinct stability classifications of landfast ice: Bottomfast ($\epsilon_a$ ~~< $1.0\times10^{-5}$~~ $\leq 8.6\times10^{-6}$), Stabilized (~~$1.0\times10^{-5} \leq$~~ $\epsilon_a^{-6} < \epsilon_a \leq$ ~~$2.3\times10^{-5}$~~ $4\times10^{-5}$), and ~~Not stabilized ($\epsilon_a$~~ Nonstabilized ($\epsilon_a$ > ~~$2.3\times10^{-5}$~~ $4\times10^{-5}$). The monthly average apparent strain decreases as the season progresses, achieving the maximum stability in April or May depending on the region. This study introduces a novel approach to identify the relative stability for areas of landfast ice using InSAR. These findings have implications for enhancing the safety and planning of activities on landfast ice for Arctic coastal communities.



## ~~1.~~ 1 Introduction

### 1.1 Remote Sensing of Landfast Ice

Landfast ice, also commonly referred to as fast ice or shorefast ice, is sea ice that has become fastened to the coast and remains stationary for a period of time (Barry et al., 1979~~).~~). Landfast sea ice is the most commonly encountered form of sea ice due to its proximity to Arctic coastal communities and its relative safety compared to drifting sea ice. Members of Arctic coastal communities use landfast ice for subsistence hunting and intercommunity travel, among other uses ~~(e.g., George et al. 2004; Laidler et al. 2009).~~(e.g., George et al. (2004); Laidre et al. (2008)). Landfast ice also serves as a habitat for marine mammals and shore birds ~~(Laidre et al. 2015; Lovvorn et al. 2018)~~(Laidre et al. (2015); Lovvorn et al. (2014)) and can be used for industrial purposes ~~(Bieniek et al. 2022; Masterson 2009).~~(Bieniek et al. (2022); Masterson (2009)). As a rigid barrier between the ocean and land, landfast ice can mitigate coastal erosion ~~(Hošeková et al. 2021)~~(Hošeková et al., 2021) and modify large-scale circulation patterns ~~(Itkin et al. 2015).~~

(Itkin et al., 2015; George et al., 2004; Laidre et al., 2008). The fundamental property of landfast ice that allows it to perform all these roles in the Earth system is its attachment to the land. Mahoney et al. ~~(2006)~~(2006) proposed that this attachment could be determined from remote sensing data using two criteria: contiguity with the coast and immobility over time. Coastal contiguity can be determined from any single image with sufficient resolution to observe meaningful leads of open water, but determination of immobility requires at least two images of the same area acquired at different times. ~~For example, Mahoney et al. (2007; 2014) analyzed triplets of co-located synthetic aperture radar (SAR) data spanning approximately 20 days to identify landfast ice in Alaska, while Fraser et al. (2009; 2012; 2021) and Cooley and Ryan (2024)~~For example,

Mahoney et al. (2007, 2014) analyzed triplets of co-located synthetic aperture radar (SAR) data spanning approximately 20 days to identify landfast ice in Alaska, while Fraser et al. (2012, 2020, 2021) and Cooley and Ryan (2024) derived landfast ice extent from 20- and 30-day composites of cloud-free moderate resolution imaging spectrometer (MODIS) data. Landfast ice is also identified in operational ice charts based on analysis of multiple images utilizing a range of satellite based sensing methods ~~(World Meteorological Organization 2024).~~(World Meteorological Organization, 2014). These various techniques of remote sensing produce similar analysis of the landfast ice in that the data is presented as a binary presence or absence of landfast ice within a grid cell. While these

~~Most remote sensing based analyses~~techniques useful and valid for mapping landfast ice, the utility of landfast ice ~~extent consider only~~does not solely rely on the ~~binary~~ presence ~~or absence~~ of ~~landfast ice, omitting other characteristics that might provide information about potential hazards associated with activities on the~~ fast ice~~. Here, we apply~~ but also the safety and stability. Interferometric Synthetic Aperture Radar (InSAR) has been shown to not only delineate landfast ice from mobile pack ice, but also measure centimeter to millimeter scale deformation within the fast ice (Dammann et al., 2016, 2018a, 2019; Dammert et al., 1998; Fedders et al., 2024; Li et al., 1996; Meyer et al., 2011; Morris et al., 1999).

### 1.2 Interferometric Coherence

Interferometric coherence ($\gamma$), derived from spaceborne sensors, is a necessary condition for processing SAR pairs using interferometry and is generally only maintained over landfast ice not mobile pack ice between repeat orbits. Interferometric coherence is the measure of correlation between the two phase signals of the same area acquired at different times (temporal baseline) and orbit positions (perpendicular baseline). Thresholding interferometric coherence to delineate landfast ice from mobile pack ice has been done before with the the L-band ($\lambda = 23.6cm$) sensor Phased Array type L-band Synthetic Aperture Radar (PALSAR) aboard the Japanese satellite Advanced Land Observing Satellite (ALOS) (Meyer et al., 2011). The low frequency of PALSAR allowed for landfast ice to maintain coherence over long periods ($\sim$ 46 days). The L-band wavelength of PALSAR allows the signal to be more resilient to decorrelating. Decorrelation, reductions of coherence, is likely the result of a combination of:

– errors in coregistration of the SAR images ($\gamma_{processes}$)

– changes in incidence angle ($\gamma_{spatial}$)

– changes in the dielectric properties of the surface ($\gamma_{thermal}$)

– and deformation of the surface ($\gamma_{temporal}$)

Examples of processes specific to sea ice which reduce coherence are redistribution of snow, melting and refreezing of the surface, ice deformation and motion, and rapid changes in salinity. Meyer et al. (2011) found that areas independently identified as mobile pack ice had an mean coherence $\leq 0.08$, indicating total decorrelation while areas of landfast ice has a mean coherence of $\sim 0.29$ with an L-band SAR sensor. This analysis lead Meyer et al. (2011) to define -pixels which maintained normalized coherence values $\geq 0.1$ over a 46 day period were classes as landfast. In addition, morphological filtering was needed to remove spurious non-contiguous pixels returning a coherence value $\geq 0.1$. Meyer et al. (2011) did note that even with L-band, coherence was poor over thin landfast ice and the after the onset of spring melt. Similarly when using the shorter wavelength C-band ($\lambda = 5.6cm$) SAR senor aboard Sentinel-1, Dammann et al. (2019) observed generally poor coherence in the along the Alaska coastline in the Chukchi Sea due to suspected thin landfast ice and surface melting. Using Sentinel-1 Dammann et al. (2019) used the boundary between zero and nonzero coherence to identify the landfast ice edge. Both Meyer et al. (2011) and Dammann et al. (2019) selected SAR pairs from winter months (December - May) to maximize landfast ice extent and thickness while reducing the impacts of melt onset thus maximizing coherence. Coherence is required to perform interferometry between two SAR signals. Without coherence, phase, and thus deformation, can not be measured accurately.

### 1.2.1 Interferometric Phase

The interferometric phase is one of the core measurements derived from interferometry as it can represented the amount of deformation which has occurred between signal acquisitions. The phase difference between SAR images is often called the

interferometric phase, $\phi$, primarily results from the effects of surface topography when viewed from two different positions, or

line-of-sight surface displacement which occurred between image acquisitions when viewed from similar positions. Over sea ice, where topographic expression is generally low, < $10m$, variations in $\phi$ can be expected to be dominated by surface motion (Bamler and Hartl, 1998; Ferretti et al., 2007). Deformation in the across-track and vertical directions result in a phase change while InSAR is not sensitive to deformation which occurs parallel to the orbit direction, also known as along-track deformation. The interferometric phase is commonly depicted by interferograms. Traditional interferograms consist of multicolored fringes where one fringe represents half a wavelength of deformation in the line-of-sight direction. The spatial rate at which the phase changes, phase gradient ($\nabla\phi$), provides insight and a measurement of the type and magnitudes of deformation occurring within the landfast ice. $\nabla\phi$ is calculated as:

$$\nabla\phi = \left(\frac{\partial\phi}{\partial x}, \frac{\partial\phi}{\partial y}\right) \quad (1)$$

indicating the change in phase in the across-track ($\frac{\partial\phi}{\partial x}$) and vertical directions ($\frac{\partial\phi}{\partial y}$). The interferometric phase (Dammert et al., 1998), fringe patterns (Dammann et al., 2018b, 2019; Fedders et al., 2024; Morris et al., 1999; Pratt, 2022; Wang et al., 2020), phase difference (Li et al., 1996), and phase gradient (Dammann et al., 2019; Fedders et al., 2024) have been used to approximate the deformation and stability of landfast ice. Inverse modeling of landfast sea ice deformation is possible from InSAR, but requires either in-situ observations of deformation and stressors or constraining the fringe patterns to specific patterns (Dammann et al., 2016, 2018a; Fedders et al., 2024). Dammann et al. (2019) classified the deformation of landfast ice based on interferometric phase on a larger scale. They opted to directly interpret the phase information as representing the magnitude of strain rather than the inverse modeling approach which would also identify the type of strain. On large scales it is not feasible to use inverse modeling to determine the type and magnitude of strain as key data to accurately constrain the each area are not available. For studies in which the deformation cannot be restricted, directly interpreting the interferometric phase as a measure of the deformation is preferred.

The classification of landfast ice stability by Dammann et al. (2019) demonstrated the utility of interpreting fringes to represent the stability of landfast ice, but the definitions used were qualitative thus difficult to reproduce and automate. Dammann et al. ~~techniques to map and classify landfast sea ice along the northern coast Alaska. Building on~~ (2019) identified three stability zones based on the interferometric fringe pattern, orientation, and spacing:

- Bottomfast ice - No identifiable phase difference from the adjacent land - same definition used by ?)
- Stabilized - Poorly defined, widely spaced fringes, or abruptly reduced fringe spacing compared to offshore ice
- Nonstabilized - Well-defined fringe orientation or patterns

While useful, these definitions can be subjective and are not easy to programmability replicate. Hence we saw a need to quantitatively defined these stability classes such that the process has the ability to be automated. We build directly on the previous work ~~(Dammann et al. 2019; Meyer et al. 2011; Pratt 2022)~~of Dammann et al. (2018b, 2019); Meyer et al. (2011); Pratt (2022) to map the extent of landfast ice and develop a method for quantitatively definition of these stability zones using interferometric data from 12 day Sentinel-1 SAR pairings.

To do so we ~~present an automatable methodology~~defined a new metric called apparent strain ($\epsilon_a$) which is derived from the interferometric phase gradient. Apparent strain describes the amount of line-of-sight deformation InSAR is sensitive too which occurred between satellite acquisitions. Having quantitative definitions of the stability zones defined by Dammann et al. (2019), using apparent strain, provides the opportunity to map the extent ~~landfast ice and identify zones~~ of ~~differing~~these stability ~~within it~~zones and ~~we use these~~ to understand ~~how the stability of landfast ice evolves over the winter.~~ their evolution both intra- and inter-seasonally.

## ~~2.~~ 2 Data and Methods

### ~~2.1.~~ 2.1 Study Area

Our study area was chosen to coincide with that used for the development of the ~~EM2024~~EM2025 landfast ice climatology (see ~~section 2.2)~~Section 2.2) and includes waters of the U.S. Arctic Outer Continental Shelf and adjacent waters in Canada and Russia. The coastlines extend from just west of Neshkan on the Chukotka Peninsula to the easternmost point of the Russian mainland in the Bering

Strait and from the westernmost point on mainland Alaska, the Iñupiat village of Wales, to the Mackenzie Delta in Canada. ~~To conform with prior analyses of landfast ice (Mahoney et al. 2007; Mahoney et al. 2014, Mahoney et al. 2024), our study area is divided into two regions (Fig. 1).~~To conform with prior analyses of landfast ice (Mahoney et al., 2007, 2014, 2024), our study area is divided into two regions (Fig. 1). The western region lies entirely within the Chukchi Sea and hereinafter is referred to as the Chukchi region~~.~~, shaded cyan in Figure 1. The eastern region includes a smaller area of the northern Alaska Chukchi coast but is otherwise contained within the Beaufort Sea and hereinafter is referred to as the Beaufort region~~.~~, blue shaded region in Figure 1. The western and eastern regions about each other at a point just west of Wainwright Alaska.

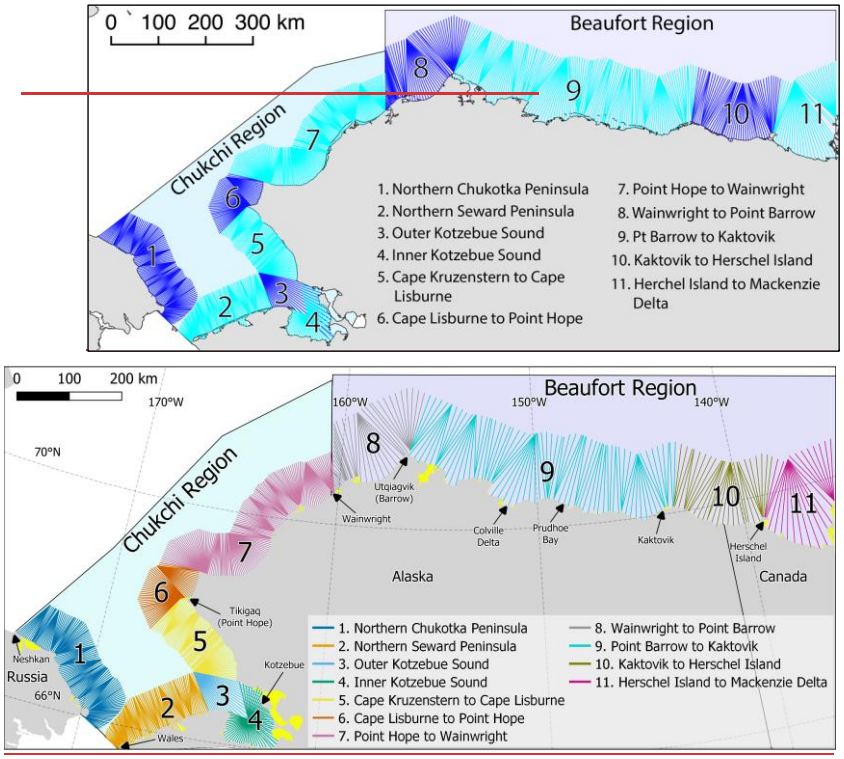


Figure ~~1.~~1. Spatial extent of the study area, two regions (Beaufort and ~~coverage of the~~ Chukchi) and 11 sub regions. Every 10$^{th}$ coast ~~vectors~~normal vector is displayed for each subregion in varying colors. Each vector is used to measure ~~landfast~~fast ice ~~width~~extent for both the InSAR method and EM2025 data.

~~EM2024~~Yellow shaded regions represent "shadow regions" discussed in Section 2.2.

## ~~2.2.~~ 115 2.2 EM2025 landfast ice climatology

The ~~EM2024~~EM2025 landfast ice climatology (named after the same authors as this study and the year it was released) is a gridded daily dataset of landfast ice extent covering the study area ~~described in section 2.1 and extending from 1996-2023. A detailed description of the creation and results of the EM2024 dataset are reported by Mahoney et al. (2024)~~depicted in Figure 1 and extends from 1996-2023. A detailed description of the creation and results of the EM2025 dataset are reported by Mahoney et al. (2024) and Mahoney and Einhorn (2025) but in brief, it extends a previous SAR-based dataset of the same study area for the years 1996-2008 ~~(Mahoney et al. 2014)~~(Mahoney et al., 2014) using data derived from ice charts produced by National Ice Center (NIC) and the National Weather Service's Alaska Sea Ice Program (ASIP). Here, we use landfast ice width data derived from the ~~EM2024~~EM2025 dataset using the SLIEalyzer toolbox ~~(https://github.com/armahoney/SLIEalyzer);~~ (https://github.com/armahoney/SLIEalyzer), which computes the distance from the coast to the seaward landfast ice edge (SLIE) along a specified set of approximately coast-normal vectors, as illustrated in Figure ~~1.~~1. Regions of the coastline which are not captured by the coast vectors are termed "shadow regions" and denoted with shaded yellow regions in Figure 1 and all subsequent maps. Shadow regions occur due to complexities of the coastline such as small bays or straits where the coast normal vector would intersect another part of the main landmass. This approach provides a consistent spatial reference frame with which to measure the seasonal and inter-annual variations in landfast ice almost continuously at 8892 different locations along the coast (6956 in the Chukchi region and 1936 in the Beaufort), spaced approximately every 200 m. It also allows us to calculate ~~average~~various statistics about the locations of the SLIE over different time periods.

## ~~2.3.~~ 2.3 InSAR-based detection of landfast ice

The term InSAR, in this study, describes a signal processing technique for calculating the phase difference between two radar signals acquired from similar locations in space at separate times. Here, we use pairs of Sentinel-1 interferometric wide (IW) beam images ~~acquired 12 days apart~~ with ~~a spatial baseline~~temporal and perpendicular baselines of ~~<~~12 days and ≤ 300 m respectively. These image pairs were selected using the Short Baseline Subset tool within the Alaska Satellite Facility (ASF)'s Vertex portal. ~~14~~13 IW reference scenes ~~were required to provide complete~~ chosen exclusively on the basis of coverage of ~~both regions in~~ the study ~~area~~region. Six reference scenes were used to cover the Beaufort region while seven were used to cover the Chukchi region. In total, 2,084 SAR pairs were identified between the months of November and July for the period from March 2017 to July 2022. ~~Multi looking by 20x4 resulted in pixel size of 80×80 m. We used ASF's Hybrid Pluggable Processing Pipeline (HyP3) toolbox (Hogenson et al., 2016) to produce interferometric data products in GeoTIFF format. The phase difference between SAR images is often called the interferometric phase, $\phi$, and primarily results from the effects of surface topography when viewed from two different positions, or line-of-sight surface displacement that occurred between image acquisitions. Over sea ice, where topographic expression is generally <10 m, variations in $\phi$ can be expected to be dominated by surface motion for the 12-day short baseline image pairs used~~

here (e.g., Dammann et al. 2016). These SAR scenes were multi-looked by 20x4 resulted in pixel size of 80×80 m, improving the signal to noise ratio. We used ASF's Hybrid Pluggable Processing Pipeline (HyP3) toolbox (Hogenson et al., 2016) to produce interferometric data products in GeoTIFF format.

To obtain a useful value of $\phi$, the surface being imaged must remain sufficiently coherent between acquisitions. Interferometric coherence describes the signal similarity, or correlation, between coregistered pixel neighborhoods in the paired images, with a value of 1 indicating perfect correlation and a value of 0 indicating complete decorrelation (Moreira et al. 2013). In the context of sea ice, coherence loss is most commonly caused by ice drift, which is typically on the order of km per day and results in the ice surface comprising a pixel to change completely within a few minutes. There are other processes unrelated to motion that reduce coherence, but if sea ice maintains coherence between image acquisitions it can be assumed to be landfast 140 To obtain a useful value of $\phi$, the two SAR signal must have remained sufficiently coherent between Sentinel-1's repeat orbits. The HyP3 toolbox (Hogenson et al., 2016) produces normalized coherence images where values of 0 indicate complete decorrelation and 1 indicates perfect coherence (Moreira et al., 2013). The magnitude of the reduction of coherence ($|\hat{\gamma}|$) can be estimated as:

$$|\hat{\gamma}| = \gamma_{processes} \cdot \gamma_{spatial} \cdot \gamma_{thermal} \cdot \gamma_{temporal} \quad (2)$$

145 By limiting our spatial baseline to ≤ 300 m and assume and use constants specific to Sentinel-1 and C-band we can treat $\gamma_{spatial}$ $\gamma_{thermal}$ as constants. In addition we assumed that $\gamma_{processes}$ is 1, indicating there are no errors in the coregistration of the SAR pairs. These assumptions allowed us to assumed all variability in the reduction of coherence was associated with deformation/displacement of the surface $\gamma_{temporal}$.

In the context of sea ice, reductions of $\gamma_{temporal}$ are assume to be caused by ice drift or deformation, which is typically on 150 the order of km per day for mobile pack ice. For drifting pack ice over a 12-day repeat orbit interval, ($\gamma_{temporal}$) is reduced to zero, resulting in decorrelation ($|\hat{\gamma}| = 0$). Fast ice by definition is stationary, but internal deformation still causes reductions of $\gamma_{temporal}$. However, for the landfast ice to remain landfast, the magnitude of this deformation needs to be relatively small as to not cause fracturing. While the coherence will be reduced in highly dynamic landfast ice, the coherence will be higher when compared to adjacent pack ice. This principle has previously been used by Meyer et al. (2011) to delineate fast ice from fast 155 land ice from pack ice.

Meyer et al. (2011) demonstrated the ability to delineate landfast ice from mobile pack ice using a coherence threshold and morphological filtering in Alaska. The normalized coherence threshold used by Meyer et al. (2011) when using L-band PALSAR was 0.1. For this study, we use C-band which is more sensitive to smaller changes in the surface resulting in lower coherence values. The coherence threshold used by Meyer et al. (2011) can not be simply assumed to be the same for the 160 different wavelengths due to the increased sensitivity of C-Band. For that reason we derived a C-Band specific coherence threshold to delineate landfast ice from mobile pack ice. A more detailed description of this derivation can be found in the

Supplementary Section A1. In short, we used 14 SAR pairs, one from each month between December 2017 and June 2018, form the Chukchi region and Beaufort region. The Chukchi scene covered most of the northern Seward Peninsula and some of Kotzebue Sound while the Beaufort region scene covered the coastline west of Utqiagvik until approximately the Colville Delta. We applied thresholds ranging from 0.01 through 1.00 to the coherence images then applied morphological closing and opening operations to remove small and noncontiguous areas which exceed the threshold which are likely noise. We then compared the areas identified by each threshold in each month to the extent of the minimum landfast ice extent identified in that month by the EM2025 dataset. The best threshold was then determined by the highest percentage of pixels that agreed with the corresponding EM2025 monthly minimum extent. The coherence threshold for delineating landfast ice from the mobile pack ice using C-Band was determined to be 0.3 where areas which meet or exceeded this threshold were classified as landfast ice. This threshold was then applied to all normalized coherence images and used to measure landfast ice extent and to mask the interferograms such that we are only calculating apparent strain in the areas identified as landfast ice.

2.4 ~~. Meyer et al. (2011) applied this concept to 45-day repeat Advanced Land Observing Satellite (ALOS) Phased Array L-band Synthetic Aperture Radar (PALSAR) data and determined that pixels with a normalized coherence value greater than 0.1 were landfast ice.~~

~~Following the work of Meyer et al. (2011), we apply the same coherence threshold identify landfast ice using from C-band Sentinel-1 imagery, under the assumption that the increased coherence from a shorter repeat orbit interval at least partially offset the reduced coherence effect of a shorter wavelength. We also apply morphological opening and closing filters to the thresholded imagery to remove small "islands" of high coherence amongst drifting ice or open water and "pinholes" of low coherence within the landfast ice. We grouped the filtered and thresholded coherence images by calendar month according to the acquisition date of the primary image in each SAR pair and mosaicked them to create monthly images of InSAR-derived landfast ice extent for each subregion. This allowed use the SLIEalyzer toolbox to obtain measurements of landfast ice width that are directly comparable with monthly means derived from the EM2024 dataset.~~

## ~~2.4.~~ Calculation of apparent strain from phase gradient

After masking the interferograms based on the ≥ 0.3 coherence threshold we used the magnitude of the interferometric phase gradient to measure the apparent strain in each interferogram. For short-baseline 12-day SAR pairs over sea ice, we can assume that variations in $\phi$ interferometric phase $\phi$ are dominated by variations in line-of-sight surface motion ~~$\phi$~~, not topography. $\phi$ is insensitive to motion perpendicular to the line of sight, but Fedders et al. ~~(2024),~~(2024), has shown that it is possible to estimate 2-dimensional horizontal strain of sea ice from the phase gradient provided the phase slope is largely planar and the mode of deformation (e.g., radial divergence or rotation) is known. However, in general, derivation of 2-D or 3-D surface motion

requires phase information from multiple look directions. and the known deformation type. Instead, we define the term apparent strain, $\epsilon_a$, to describe the magnitude of the horizontal gradient in line-of-sight displacement. Apparent strain can be calcuated using the following:

$$\epsilon_a = \frac{\lambda}{4\pi(pixel\ width)}|\nabla\phi| \quad (1)$$

$$\epsilon_a = \frac{\lambda}{4\pi(\text{pixel width})}|\nabla\phi| \quad (3)$$

Where $\lambda$ is the C-band SAR wavelength (5.64 cm) of Sentinel-1 and $|\nabla\phi|$ is the magnitude of the phase gradient, given by:

$$|\nabla\phi| = \frac{\sqrt{\frac{\partial\phi}{\partial x}^2 + \frac{\partial\phi}{\partial y}^2}}{(kenral\ length - 1)} \quad (2)$$

$$|\nabla\phi| = \frac{\sqrt{\frac{\partial\phi}{\partial x}^2 + \frac{\partial\phi}{\partial y}^2}}{(kenral\ length - 1)} \quad (4)$$

Since $\phi$ is a cyclic quantity that wraps over an interval of $2\pi$, we calculate $\nabla\phi$ following the approach described by Libert et al. (2022) whereby $\phi$ is first converted to a complex quantity, $\phi^*$, with continuous real and imaginary components:

$$\phi^* = e^{i\phi} = cos\phi + i\,sin\phi \quad (3)$$

$$\frac{\partial\phi}{\partial x} = \angle\left(\frac{\partial\phi^*}{\partial x}\right) \quad (4)$$

$$\frac{\partial\phi}{\partial y} = \angle\left(\frac{\partial\phi^*}{\partial y}\right) \quad (5)$$

$$\phi^* = e^{i\phi} = cos\phi + i\,sin\phi \quad (5)$$

$$\frac{\partial\phi}{\partial x} = \angle\left(\frac{\partial\phi^*}{\partial x}\right) \quad (6)$$

$$\frac{\partial\phi}{\partial z} = \angle\left(\frac{\partial\phi^*}{\partial z}\right) \quad (7)$$

Where $\angle$ indicates the argument of the complex exponent.

We approximate the partial derivatives in (4) and (5)(Eq.6) and (7) using finite differences across a 4-pixel window and insert into (2)(Eq.

195 4) to derive the magnitude of the phase gradient magnitude. Apparent strain, ~~$\epsilon_a$~~$\epsilon_a$, is then calculated using ~~(1)~~(Eq. 3) and should be interpreted as the minimum net strain that occurred between SAR image acquisitions, since it only measures deformation along the satellite's line of site. However, since it only represents displacement between two snapshots in time, it may underestimate the maximum strain that occurred during the 12-day period. As with the coherence images, we grouped ~~$\epsilon_a$~~$\epsilon_a$ results by month according to the date of the primary image in each SAR pair and mosaicked results to create images of monthly average ~~$\epsilon_a$~~$\epsilon_a$ for 200 each of the Chukchi and Beaufort regions~~. Pixels with a coherence <0.1 were excluded from the results~~.

## ~~2.5.~~ 2.5 Spatial masks for defining apparent strain thresholds for stability ~~classes~~

~~Dammann et al. (2019) used InSAR to define three classes of stability within landfast ice, based on a qualitative analysis of the density and orientation of interferometric fringes: bottomfast, stabilized, and non-stabilized. Bottomfast ice is the most stable of these classes and occurs in water shallow enough where the entire water column freezes, and the sea ice is frozen too or is resting on the seafloor. This depends on the ice thickness (or, more precisely, the draft of the ice), but in our study region bottomfast ice will be found in waters up to approximately 1.5 m deep (Pratt 2022). In interferograms, bottomfast ice was identified based on "*No identifiable phase difference from the adjacent land*". Stabilized landfast ice is found seaward of the bottomfast ice zone where the ice is floating but held in place by islands or grounded pressure ridges~~The Sentinel-1 SAR pairs using by Dammann et al. (2019) along the Alaskan Beaufort coastline do not follow the same strict temporal baseline requirement of 12-days between pairs prohibiting the direct use of these SAR pair during the derivation of apparent strain thresholds for each stability class, but will be used to compare with later. To account for this, we interpreted the 205 landfast ice regimes associated with each stability zone and created masks that reflect the characteristics of landfast ice in each zone, but are usable in all years (Fig. 2). The spatial extents for each of these masks was determined independently of apparent strain values but instead by bathymetry, geomorphology characteristics, and features of the nearshore environment. These masks, which are shown in Figure 2, represent the areas we know to fit the characteristic of each fast ice regime associated with each stability zone defined by Dammann et al. (2019). These stability zones were defined using the following criteria 210 associated with bathymetry, geomorphology characteristics, and features:

1. Bottomfast Landfast Ice (BFLFI) - Areas of the near shore environment with a water depth shallower than 1.5 m (Danielson et al., 2015)

2. Sheltered Landfast Ice (SHLFI) - Areas between the seaward edge of the BFLFI edge and shoreward of any barrier island. We acknowledge that barrier islands are not the only feature which anchor landfast ice.

215 3. Not Sheltered Landfast Ice (NSHLFI) - Areas where landfast ice occurs seaward of barrier island.

The bounds of the BFLFI mask were determined to be the area where water depth is between 0 m and 1.5 meters as these are the typical depth bottomfast ice is found (Pratt, 2022). It is also important to acknowledge the difference between sheltered and stabilized terminologies in this instance. Sheltered landfast ice (SHLFI) is specifically landfast ice which is floating and anchored by barrier islands. The barrier islands shelter this landfast ice from dynamic interactions with waves and pack ice.

SHLFI is likely to exhibit greater stability (lower apparent strain) compared to landfast ice anchored by grounded ridges, as barrier islands can better isolate landfast ice from ocean dynamics. The definition of the stabilized landfast ice zone by Dammann et al. (2019) includes landfast ice anchored by both barrier islands and grounded ridges. However, due to the location of grounded ridges not being consistent between seasons, we opted to use the areas sheltered only by barrier island, SHLFI, as a representative area for the determination of an apparent strain threshold of the stabilized zone defined by Dammann et al.

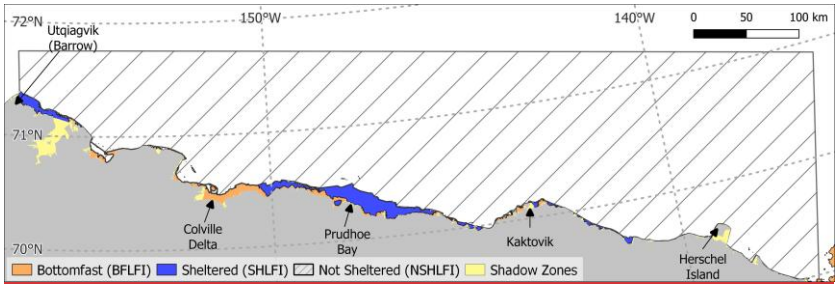


Figure 2. Spatial extent of the masks use for the derivation of the apparent strain thresholds associated with the stability zones from Dammann et al. (2019). Orange areas are bottomfast, blue is sheltered, and hashed black is not sheltered. Yellow shaded regions represent "shadow regions" discussed in Section 2.2.

(2019). Given this definition and spatial extent of SHLFI, we can assume that any landfast ice occurring within the SHLFI mask is anchored, thus representative of stabilized landfast ice, regardless of season. This also results in landfast ice that is grounded by ridges seaward of the barrier island to be located within the NSHLFI mask, skewing the distribution of the NSHLFI toward a lower apparent strain. We then took the average of all apparent stain maps, on a per pixel basis, occurring in the Beaufort region during the month of April and derived the apparent strain thresholds for the three stability zones defined by Dammann et al. (2019) using a non-parametric optimization of the data within each mask independently.

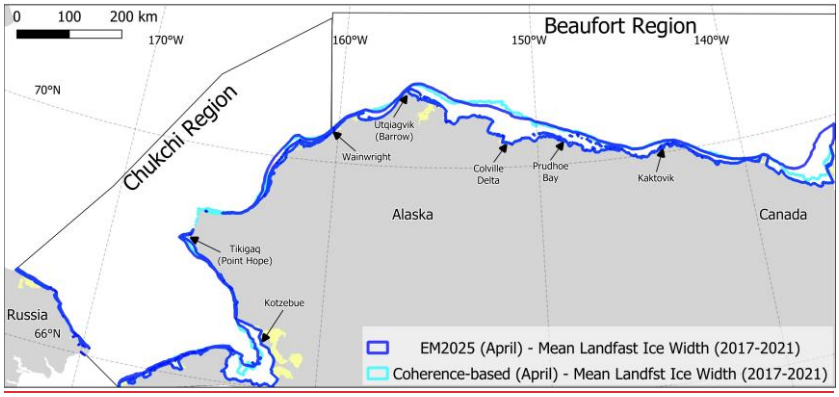


Figure 3. Spatial comparison of the April monthly mean (2017-2021) landfast ice width across the study region using the coherence based mosaics (cyan) and the EM2025 dataset (blue). Yellow regions are "shadow zones" where the coast vectors do not reach.

3 ~~, Dammann et al. (2019) identified stabilized ice based on "*Poorly defined, widely spaced fringes, or abruptly reduced fringe spacing compared to offshore ice*". Lastly, non-stabilized ice includes all landfast seaward of any island or grounded ridge and was identified according to "*Well-defined fringe orientation or patterns*".~~

~~To quantitatively define apparent strain thresholds associated with each of these stability classes, we created the following three non-overlapping spatial masks within the Beaufort study region:~~

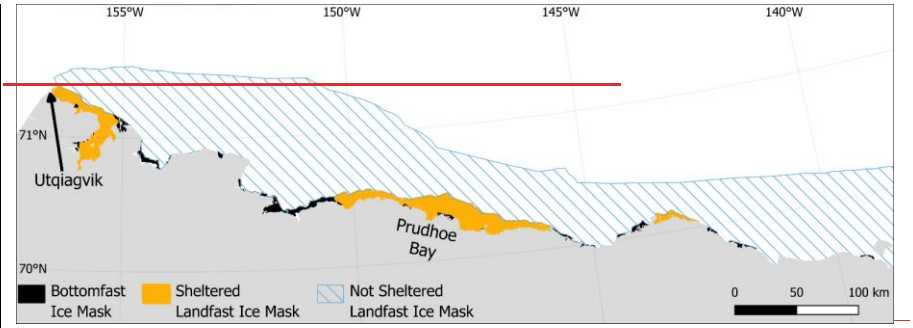


**~~Figure 2: Spatial extent of bottomfast, sheltered, and not sheltered landfast ice masks~~**

1. ~~Bottomfast ice mask. This corresponds to the area identified as bottomfast by Dammann et al. (2019) (black in Fig. 2). The maximum extent of bottomfast ice extent along the Beaufort coast varies little enough between seasons (Pratt 2022) that we can use the bottomfast ice extent defined during April of 2017 by Dammann et al. (2019) to identify the areas which are likely bottomfast ice during April of all seasons.~~
2. ~~Sheltered ice mask: This is defined by the area seaward of the bottomfast ice mask and shoreward of any barrier islands (orange areas in Fig. 2). This represents floating landfast ice that can be expected to be sheltered from dynamical interaction with pack ice by the islands and should therefore be representative of stabilized ice.~~
3. ~~Not-sheltered ice mask: This is the area seaward of any barrier islands (light blue hashed areas in Fig. 2) and will include all the landfast ice subject to dynamical interaction with pack ice. However, it may also include grounded pressure ridges and so we expect the non-sheltered ice mask to represent both non-stabilized and stabilized landfast ice.~~

## ~~3.~~ Results

### ~~3.1.~~ 3.1 Landfast ice extent from coherence thresholds

Application of the coherence threshold described in ~~section 2.3~~Section 2.3 to 2,084 SAR image pairs allowed us to produce ~~24~~30 monthly ~~images~~mosaics of landfast ice for each month between December and May during the ~~4~~5 landfast ice seasons between 2017 and 2021.

235 We then used the SLIEalyzer toolbox (~~section~~Section 2.2) to derive the average position of the SLIE over all ~~4~~5 seasons for each month for comparison with the equivalent results derived from the ~~EM2024~~EM2025 dataset from these. For example, ~~Fig. 3~~Figure. 3 compares positions of the InSAR-derived mean landfast ice extent during April (~~cyan~~blue) line with that derived from the

~~EM2024~~EM2025 dataset (~~blue~~cyan) for the period 2017~~—~~2021. This shows a generally good agreement, with no consistent bias ~~across~~in the study region for this month. However, when averaging the difference between methods, the coherence mosaics did tend to slightly underestimate the landfast ice extent in each month.

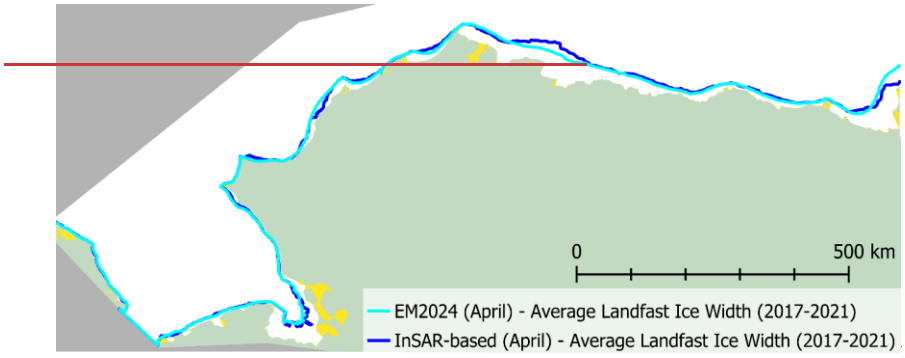


~~**Figure 3: Mean SLIE position for the month of April by the EM2024 dataset (cyan) and InSAR-based method (blue) from 2017 – 2021. Yellow regions indicate "shadow" zones outside the domain of the coast vectors (see Fig. 1)**~~

To compare the ~~InSAR~~coherence-derived landfast ice extent against the ~~EM2024~~EM2025 dataset for all months from December to May, we calculated the difference in monthly mean landfast ice width for each coast vector ~~(Fig. 4).~~measured by the coherence-based method and the EM2025 dataset (Fig. 4). Here, the difference ~~(blue line)~~ is calculated by subtracting the ~~InSAR-derived width~~EM2025 values from the ~~EM2024 values. The normalized difference (gray line) is~~ coherence-derived ~~by dividing the difference by the EM2024~~ width~~.~~ values, meaning a negative value represents an underestimate by the coherence method. Figure 4 represent then entire coastline where coast vectors from the Chukchi region are plotted in cyan while the Beaufort is in blue. During December~~,~~ (Fig. 4A), mean landfast ice width was zero throughout much of the study region and both datasets generally agree where landfast ice had not yet formed~~, but small differences in width result in large, normalized differences.~~ However, where landfast was present (primarily in the Beaufort region), the InSAR-derived results tend ~~to underestimate the width. This is illustrated by the tendency of the blue line to lie below the x-axis in Fig. 4a.~~

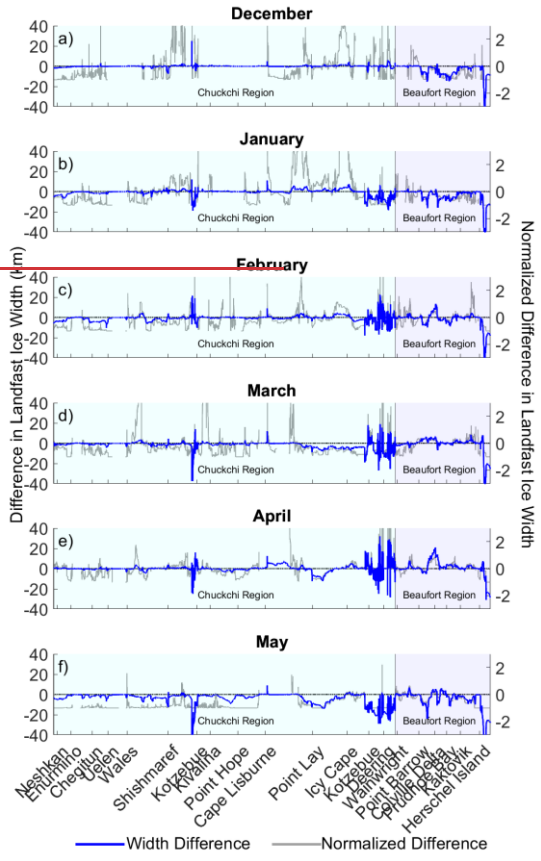


**Figure 4: Difference in landfast ice width at each coast vector from 2017–2021 between the InSAR-derived results and the EM2024 dataset. Positive values indicate that the InSAR method overestimate landfast ice extent relative to the EM2024 dataset. Cyan shaded regions were within the Chukchi region and blue shaded regions were the Beaufort region.**

to underestimate the width. On average in the Beaufort region during December the coherence method measured 5.1 km less landfast ice at each coast vector. This is illustrated by the tendency of the blue line to lie below the black line, where the black line indicates a difference of 0 in Figure 4A.

There is a similar pattern for the month of January (Fig. ~~4b~~4B), with the InSAR-based approach still tending to underestimate the width of landfast ice as it expands throughout both study regions. ~~However as the season progresses through~~The tendency to underestimate persist until mid-winter, February, March, and April, where the relationship becomes more variable along the coast, with the InSAR-based approach indicating over 10 km more landfast ice than the ~~EM2024~~EM2025 dataset at certain coast vectors (Fig. ~~4b-c).~~4C-E). Although the average differences remain negative during the mid-winter months, with values of -5.1 km, -4.6 km, and -3.4 km from February to April in the Beaufort region, and -2.5 km, -3.7 km, and 1.5 km in the Chukchi region, these differences constitute only small percentages of the total average landfast ice during this period. Also, there is notable spatial variability ~~in~~within the subregion Inner Kotzebue Sound during these months, with the difference in landfast ice width changing from ~~<~~ ~~10~~<−10 km to >10 km and back again over the span of just a few coast vectors. The cause of this variability is not certain, but examination of the parent SAR imagery and interferograms over Kotzebue Sound indicate that the surface of the ice loses coherence temporarily without any substantial horizontal motion. This coherence loss could be caused by surface flooding, which has been observed to be caused by heavy snow load in this region ~~(Mahoney et al. 2021).~~(Mahoney et al., 2021). Kotzebue Sound also has extensive areas of shallow water ~~(~ ≤~~(~≤2 m), in which the ice can repeatedly interact with the seafloor as the water level rises and falls under the influence of winds and tides. This process can result in ~~flexural~~flexure fracturing of the ice surface, which can also lead to coherence loss. Similar observations of poor coherence using C-band SAR over Kotzebue sound were made by Dammann et al. (2019).

In the month of May~~,~~ (Fig. 4F), the landfast ice width difference between the two datasets is more consistently negative ~~again,~~. In the Beaufort region the coherence based method measured on average 10.7 km less landfas ice extent during May. Similarly the in the Chukchi region the coherence method measured 5.4 km less than the EM2025. The differences are due to extensive areas where no landfast ice was identified by the ~~InSAR~~coherence-based method, but landfast ice was still present in both the Chukchi and Beaufort coasts in the ~~EM2024~~EM2025 dataset. In particular, Kotzebue Sound never met the coherence threshold to be considered landfast ice during May of any season from 2017~~–2021. This consistent underestimation by the InSAR-based method is likely due to the alteration of the dielectric properties of the ice surface during the early stages of melt, which leads to the loss of coherence before any substantial motion of the ice.~~ -2021. Surface melting is the likely cause of this underestimate and highlights the limitations of using coherence to identify landfast ice outside of the winter months.

## ~~3.2.~~ 3.2 Monthly mean apparent strain

Although there is considerable variability in monthly mean ~~$\epsilon_\alpha$~~$\dot{\varepsilon}_a$ at the scale of adjacent pixels, we identify an overall tendency for lower ~~$\epsilon_\alpha$~~$\dot{\varepsilon}_a$ values to be found near the coast and higher values to occur nearer the SLIE (Fig. ~~5~~5 and ~~6).~~6). This spatial distribution becomes more evident as the landfast ice season progresses and another tendency emerges whereby the apparent strain in landfast ice tends to decrease over time. ~~By calculating probability distribution of monthly $\epsilon_\alpha$ values , we find that the modal value of $\epsilon_\alpha$ decreases monotonically from December to May (Fig. 7). This indicates that landfast ice becomes more stable the longer it persists.~~Both Figure 5 and 6 are a representation of the mean seasonal progression of landfast ice extent and apparent strain values within the study region. The inset of each figure, denoted by a lowercase A, is a zoomed in view near Utqiagvik, Alaska. Dark blue areas indicate very stable landfast ice, low apparent strain, while yellow indicates

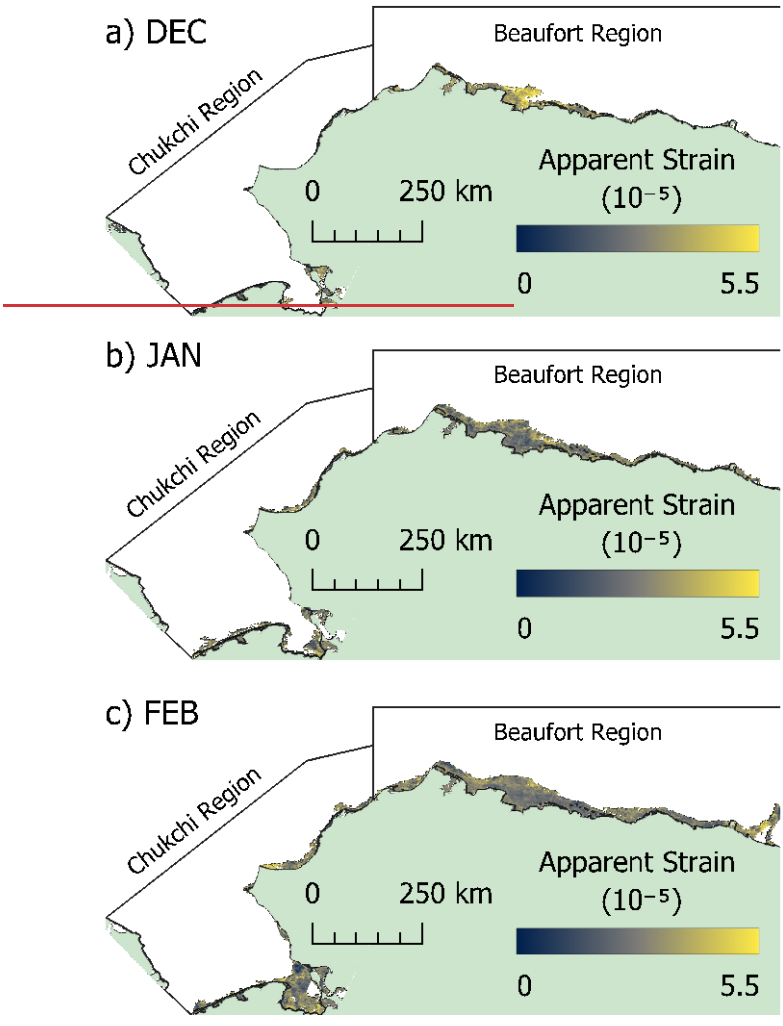
a) DEC
Beaufort Region
Chukchi Region
0
250 km
Apparent Strain
(10⁻⁵)
0
5.5
b) JAN
Beaufort Region
Chukchi Region
0
250 km
Apparent Strain
(10⁻⁵)
0
5.5
c) FEB
Beaufort Region
Chukchi Region
0
250 km
Apparent Strain
(10⁻⁵)
0
5.5

~~Figure 5: Monthly mean~~280 relatively less stable landfast ice, high apparent strain (Fig. 5 and 6). The transition from ~~2017–2021 for~~yellow to green to blue, high to low apparent strain, within Elson lagoon throughout the winter months indicates an increase in stability the longer the landfast ice

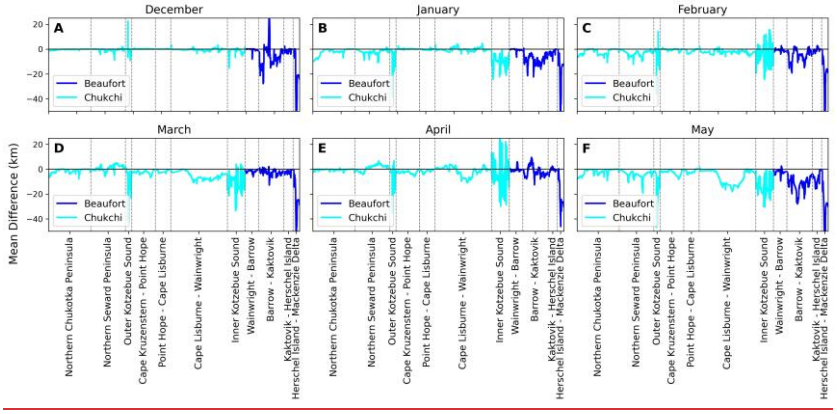


Figure 4. Difference of ~~a)~~monthly average landfast ice width measured by the EM2025 dataset and the coherence-based method from 20172021 in December~~, b) January, and c) February~~ through May. Negative values indicate an under estimate by the coherence-based method. Cyan indicated the measurements occurred in the Chukchi region while blue is the Beaufort region. Vertical dashed gray lines indicate the bounds of the subregions shown in Figure 1.

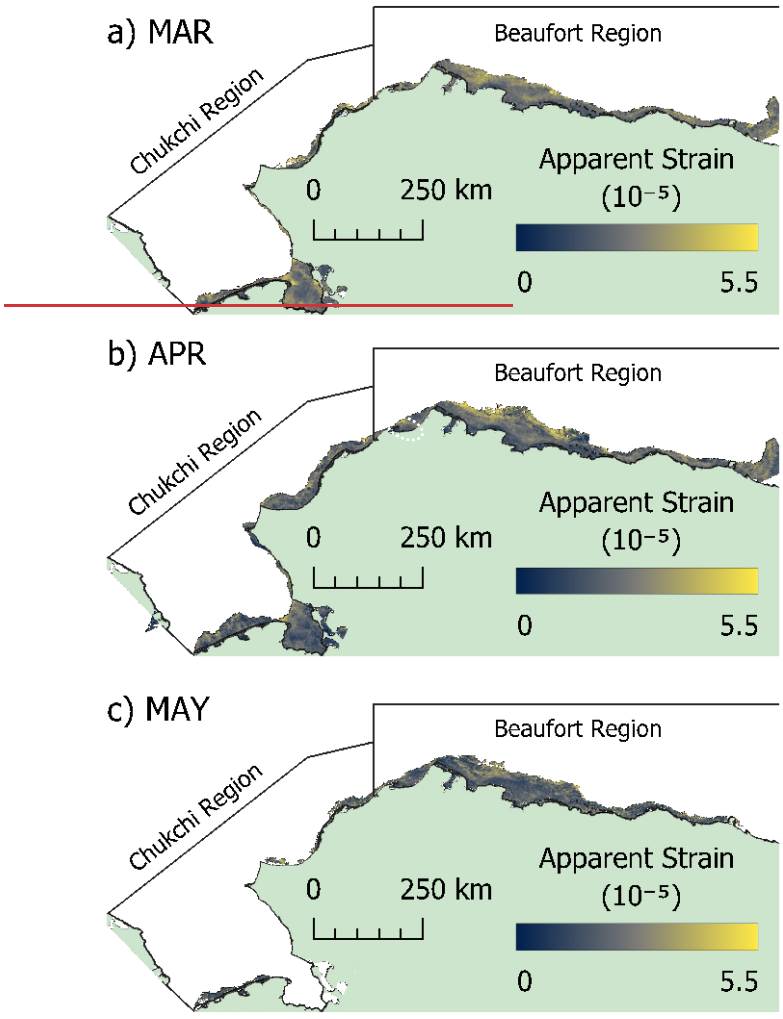
a) MAR
Beaufort Region
Chukchi Region
0
250 km
Apparent Strain
(10⁻⁵)
0
5.5
b) APR
Beaufort Region
Chukchi Region
0
250 km
Apparent Strain
(10⁻⁵)
0
5.5
c) MAY
Beaufort Region
Chukchi Region
0
250 km
Apparent Strain
(10⁻⁵)
0
5.5

~~Figure 6: Monthly mean apparent strain from 2017–2021 for the months of a) March, b) April, and c) May~~

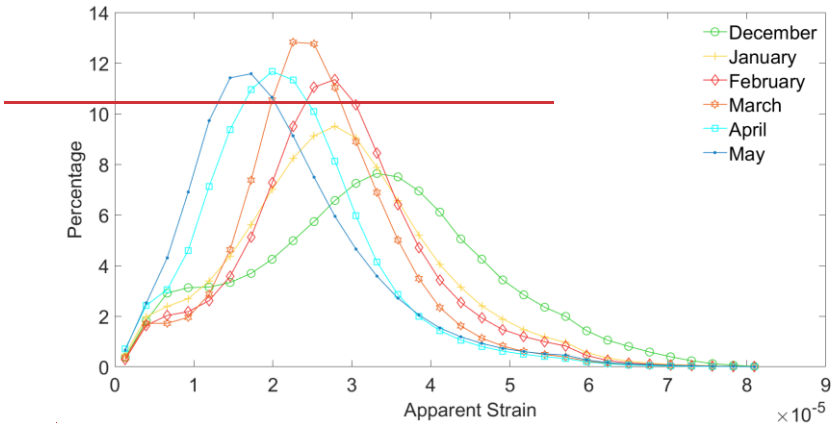


~~**Figure 7: Distribution of average apparent strain during each month (December, January, February, March, April, and May) between 2017–2021**~~

persists (Fig. 5Aa-Ca and 6Aa-Ca). By calculating probability distribution of monthly $\epsilon_a$ values , we find that the modal value of $\epsilon_a$ decreases monotonically from December to May (Fig. 7). During the month of May, very few pixels within the Chukchi region met the coherence threshold (Fig. 6C). And in both regions, areas of landfast ice did not meet the coherence threshold to be considered landfast ice during the month of June thus the distributions were omitted. The inability to identify landfast ice during formation and after the onset of melt is a major flaw with this method, however the method works throughout the winter months as demonstrated proving the usefulness.

### ~~3.3.~~ 3.3 Quantitative classification of landfast ice stability

In the Beaufort Sea, landfast ice typically reaches its seasonal maximum width during April ~~(Mahoney et al. 2014).~~(Mahoney et al., 2014). This is also the month for which Dammann et al. ~~(2019)~~(2019) qualitatively defined landfast ice stability throughout the Arctic based on interferometric phase gradient. Hence, we use our monthly mean $\epsilon_a$ values for the month of April to derive the probability distributions of $\epsilon_a$ within the three ~~spatial masks~~stability zones identified in ~~Fig. 2, corresponding to~~ Figure 2. The distributions of apparent strain in each stability zone bottomfast, (orange), sheltered, (blue), and not- sheltered ~~ice (Fig.~~

8). Each(black) are shown in Figure 8). The bottomfast region has a bimodal distribution has a while the sheltered and not sheltered zones have a well-defined and distinct mode, with themodes. The modal apparent strain value for the bottomfast ice mask beingis the lowest and that for the not-sheltered ice beingis the highest. The bimodal distribution of apparent strain values within the highest.bottomfast stability zone is likely the associated with tide cracks, which form at the oceanward

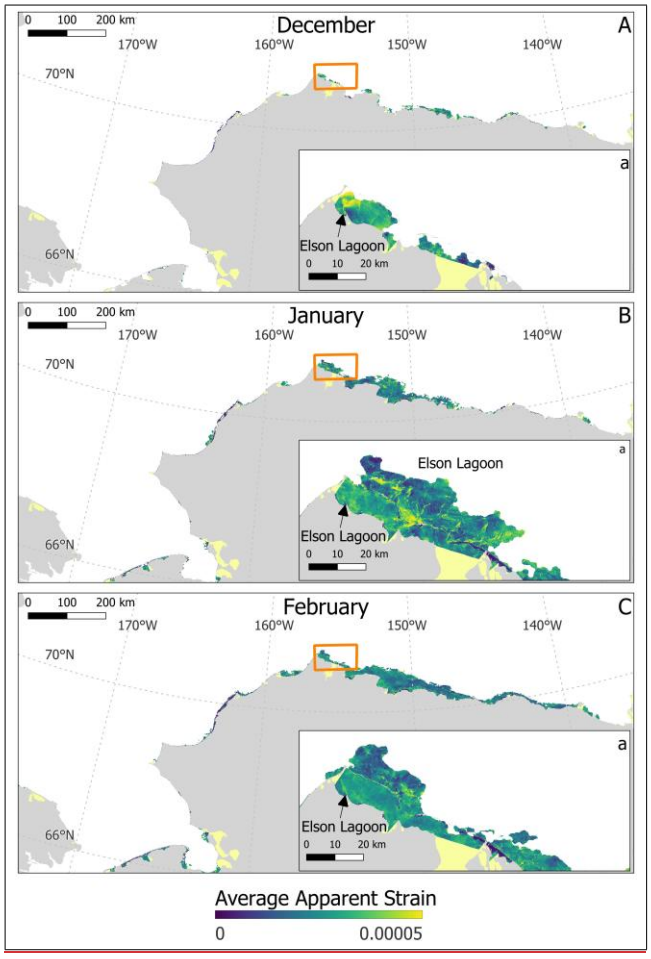
December
A
January
B
February
C
0 100 200 km
170°W
160°W
150°W
140°W
70°N
66°N
a
Elson Lagoon
0 10 20 km
Average Apparent Strain
0
0.00005

Figure 5. Monthly mean apparent strain values for December (A), January (B), and February (C) for both Beaufort and Chukchi regions from 2017-2021. The orange box denotes the extent of inset figure in each (a). Dark blue areas mark low apparent strain regions while yellow denotes high apparent strain.

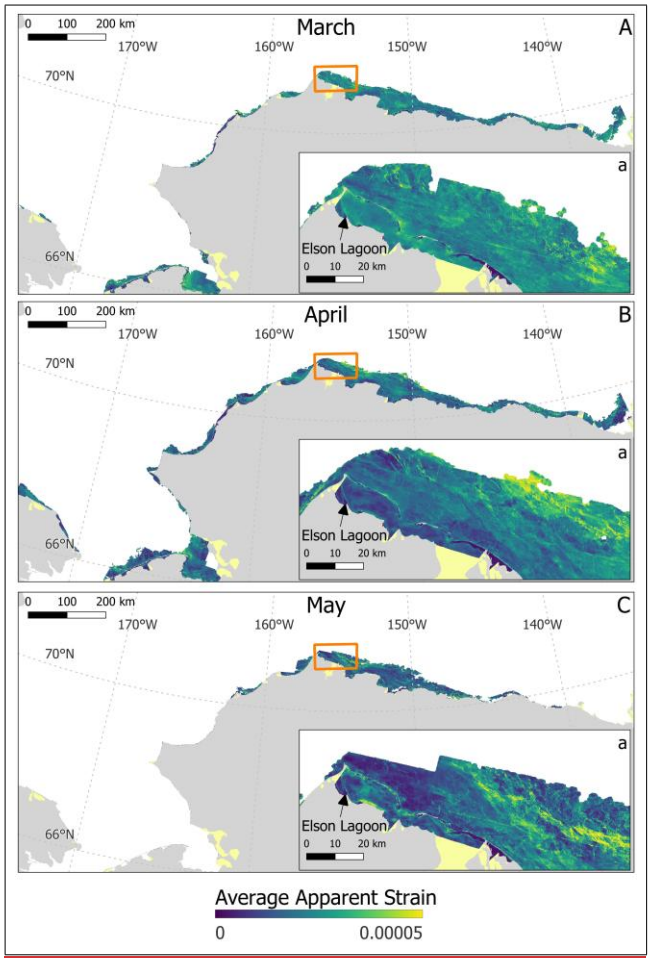
March
A
April
B
May
C
0 100 200 km
170°W
160°W
150°W
140°W
70°N
66°N
a
Elson Lagoon
0 10 20 km
Average Apparent Strain
0
0.00005

Figure 6. Monthly mean apparent strain values for March (A), April (B), and May (C) for both Beaufort and Chukchi regions from 20172021. The orange box denotes the extent of inset figure in each (a). Dark blue areas mark low apparent strain regions while yellow denotes high apparent strain.

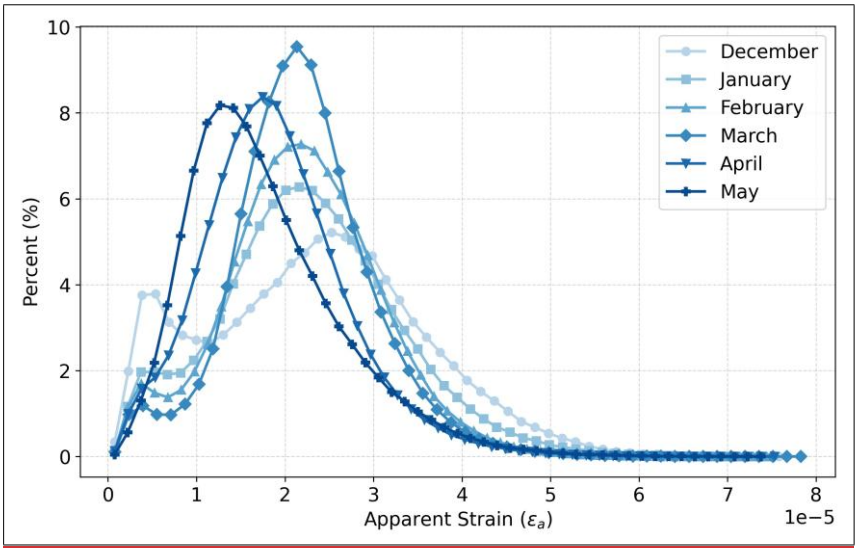


Figure 7. Distribution of the monthly mean apparent strain values from December through May for all pixels within the study region from 2017-2021.

boundary of bottomfast ice. The distributions for sheltered and not-sheltered ice are approximately normally distributed~~, but the bottomfast ice distribution is right skewed, which~~ with considerable overlap which is expected as we assume the not sheltered region contains landfast ice which is stabilized by grounded ridges. We then applied Otsu's algorithm (Otsu, 1979) to the distributions of apparent strain in each stability zone

300 independently to determine the apparent strain thresholds associated with each stability zone. The apparent strain threshold for the bottomfast ice stability zone was determined to be $\epsilon_a = 8.6\times10^{-6}$, marked by a yellow dashed line in Figure 8. For the sheltered and not sheltered regions the thresholds were determined to be $\epsilon_a = 1.8\times10^{-5}$ and $\epsilon_a = 2.4\times10^{-5}$ marked by blue and black lines respectively (Fig. 8). However, we only need a single threshold to differentiate sheltered from not sheltered landfast ice. As we have assumed that stabilized landfast ice exists within the not sheltered region, stabilized by grounded

ridges, we interpret the Otsu threshold for the not sheltered region to represent the apparent strain threshold for delinting landfast ice which is stabilized by a feature (i.e. barrier island or grounded ridge) and the nonstabilized landfast ice. We now have two apparent strain thresholds that determine the apparent strain bounds for three stability classes:

1. Bottomfast: $\epsilon_a \leq 8.6\times10^{-6}$

2. Stabilized: $8.6\times10^{-6} < \epsilon_a \leq 2.4\times10^{-5}$

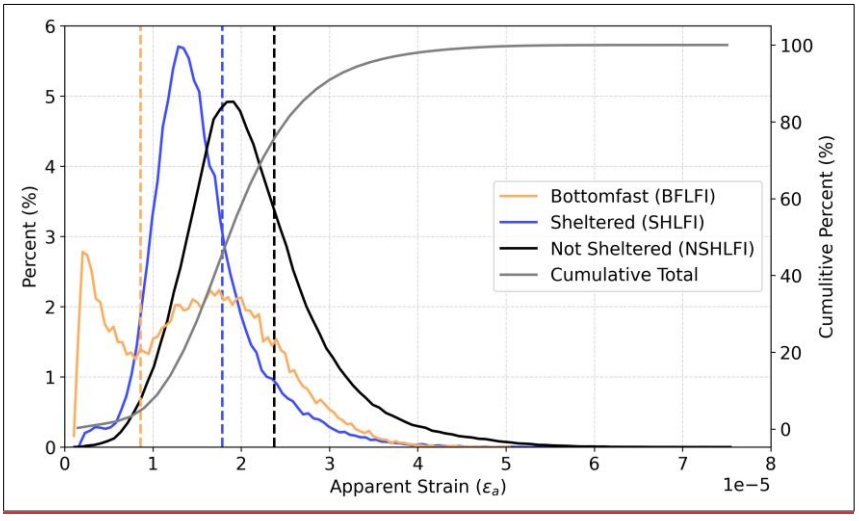


Figure 8. Distribution of the average apparent strain values from April 2017-2021 in each stability zone defined in Figure 2(solid lines). Dashed lines indicate the value of the Otsu threshold for each stability zone.

3. Nonstabilized: $\epsilon_a > 2.4\times10^{-5}$

To test our apparent strain thresholds, we calculated the apparent strain of the interferograms used by Dammann et al. (2019) along the Beaufort coastline and compared the extents of our quantitatively defined stability classes to those defined by

Dammann et al. (2019). Apart from the method of stability classification, qualitative by Dammann et al. (2019) vs quantitative, Dammann et al. (2019) did not enforce a strict temporal baseline for the SAR pairs and they used a non-zero coherence value

to identify the seaward landfast ice edge (SLIE). The three Sentinel-1 SAR pairs used by Dammann et al. (2019) were: April 8th, 2017 – May 2nd, 2017; April 15th, 2017 – May 9th, 2017; and April 17th, 2017 – April 29th, 2017. The interferograms produced from these SAR pairs and the resulting apparent strain maps can be seen in Figures 9A/B. The interferograms show the extents of the stability zones defined by Dammann et al. (2019) with the areas outlined by red identified as bottomfast, purple stabilized and cyan nonstabilized (Fig. 9A). Once the thresholds were applied to the apparent strain maps we directly compared how the qualitative and quantitative methods compared (Fig. 9C). The main difference between the methods is the extent of the nonstabilized landfast ice. The higher coherence threshold used in this study, $\gamma \geq 0.3$, compared to the non-zero requirement by Dammann et al. (2019), resulted in an underestimate of the landfast ice extent. However, the transition from stabilized to nonstabilized is captured well (Fig. 9Ca). In addition, the areas which are classed as bottomfast are separated from near by stabilized landfast ice by a thin area of nonstabilized ice. We believe this area of high apparent strain is associated with tide cracks as they present as high strain over a relatively short area. To further investigate the performance of the apparent strain thresholds, we produced a confusion matrix of the classification types by Dammann et al. (2019) vs this studies apparent strain classes (Table 1). The nonstabilized class is the only class where both methods agreed on the majority of pixels which met the ≥ 0.3 coherence threshold (Table 1). We believe the classification disagreement, where the apparent strain indicated bottomfast ice while Dammann et al. (2019) stabilized is the result of ~~high $\epsilon_a$ values being present at the oceanward bottomfast ice boundary, likely associated with tide cracks.~~ multiple grounded ridges in a small area. Both of the

~~To define the $\epsilon_a$ thresholds that separate the three stability classes initially put forward by Dammann et al (2019) (see section 2.3), we use the lower and upper 10th percentiles of $\epsilon_a$ values found within sheltered ice mask. The lower 10th percentile corresponds to a value of apparent strain of $1.0\times10^{-5}$ and closely coincides with the intersection between the sheltered ice and bottomfast ice distributions. $\epsilon_a$ values lower than this are therefore more likely to be found in the bottomfast ice mask than in the sheltered ice mask. The 90th percentile of the sheltered ice distribution corresponds to an apparent strain of $2.3\times10^{-5}$. We note that this aligns with the mode of the not-sheltered distribution, rather than intersection between the sheltered and not-sheltered distributions. However, we expect that areas in the not-sheltered region may still have been stabilized, but by a grounded ridge rather than a permanent barrier island. This likely explains why the mode of the not-sheltered region is broader and is why we did not choose the intersection point of the sheltered and non-sheltered distribution as the threshold between stabilized and non-stabilized ice. These apparent strain thresholds can now be applied to results from single interferograms to identify areas of varying stability within the landfast ice.~~

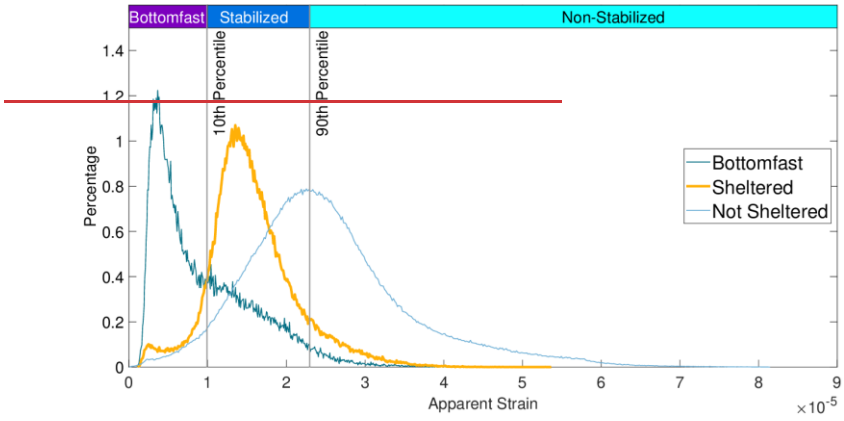


~~Figure 8. Distribution of April mean apparent strain, $\epsilon_{\bar{a}}$, during the period 2017–2021 in the areas identified as bottomfast, sheltered, and not-sheltered landfast ice.~~

330 regions of large misclassifications, west of the Colville Delta and north of Prudhoe Bay (Fig. 9C), have been identified as common areas for grounded ridges to occupy (Lange et al., 2024). Thus we do not view the disagreement of classification as wrong, just that there are various processes can reduce apparent strain, and in the right conditions, produce very stable landfast ice.

| | Apparent Strain Class |
|---|---|

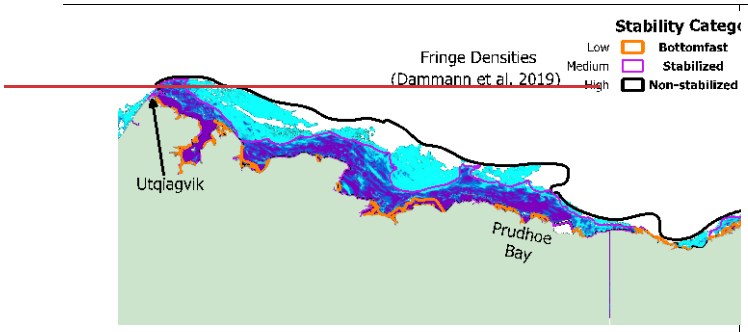


Figure 9: Categorized landfast ice stability derived from apparent strain threshold applied to interferograms from April 2017 corresponding to those used by Dammann et al. (2019). Orange, purple and black lines indicate the extent of the stability regions defined by Dammann et al (2019), bottomfast, stabilized, and not stabilized. Dark purple, blue and cyan shaded regions correspond to pixels which had apparent strain values within the quantitatively defined stability categories: bottomfast, stabilized and not stabilized.

Bottomfast

Stabilized

Nonstabilized

Inserted Cells

Dammann et al. Class

| | | | |
|---|---|---|---|
| Bottomfast | 41.8 | 33.4 | 24.8 |
| Stabilized | 28.1 | 46.6 | 25.3 |
| Nonstabilized | 3.6 | 22.8 | 73.6 |

Table 1. Percentages of landfast ice classification types the based on qualitative characteristics by Dammann et al. (2019) and apparent strain thresholds for SAR pairs displayed in Figure 9A.

We applied the thresholds illustrated in Fig. 8 to $\epsilon_a$ values derived from SAR pairs acquired in April 2017 similar to those used by Dammann et al. (2019) along the Beaufort coast in Alaska. The exact SAR pairs used by

4 Dammann et al. (2019) were not available through ASF's Vertex portal and so we selected overlapping pairs that were acquired within 12 days. This allows us to directly compare the extents of each stability class determined from our $\epsilon_a$ thresholds with those manually delineated by Dammann et al (Fig. 9). Overall, the boundary between stabilized and non-stabilized landfast ice agrees between the methods suggesting that our $\epsilon_a$ threshold of $2.3\times10^{-5}$ derived from 4-year monthly averages can be usefully applied to data from individual SAR pairs. Damman et al (2019) did not apply a rigorous coherence threshold and identify a greater extent of landfast ice extent in some areas, but otherwise both methods show good agreement on the position of the SLIE. However, there is a large discrepancy in area identified as bottomfast ice, which

~~we attribute to abnormally low apparent strain in regions behind barrier islands at this particular time. The $c_a$ values throughout Elson lagoon are considerably lower than the mean value for this month (Fig. 6) and fall within range typically found in bottomfast ice.~~

## ~~4.~~ Discussion

### ~~4.1.~~ 4.1 Suitability of InSAR for routine identification of landfast sea ice

In general, landfast ice extent is captured well using ~~InSAR~~interferometric coherence during the winter months of the landfast ice season but under-identifies landfast ice extent at the beginning or end of the season. Despite the typical presence of landfast in both the Chukchi and Beaufort regions during November ~~(Mahoney et al. 2024), we did not find any pixels outside the land mask with a coherence values <0.1 until December, representing a total underestimate of landfast ice during the earliest stage of formation. We attribute the loss of coherence over immobile~~and June (Mahoney et al., 2024; Mahoney and Einhorn, 2025), we did not find any pixels outside the land mask with a coherence values ≥ 0.3 until December or after May. The coherence-based method does not capture landfast ice extent during the begging and end of the landfast ice season, two important parts of the season when discussing changes between seasons. In the early winter, we attribute the loss of coherence over immobile landfast ice to the rapid changes in the dielectric properties of the ice surface that occurred during early stages of growth ~~(e.g., Winebrenner et al. 1996).~~(e.g., Winebrenner et al. (1996)). During the months of December and January, the average the monthly width of landfast ice identified by our ~~InSAR~~coherence based method ~~is slightly less than~~under represents compared to the ~~average monthly landfast ice width from the EM2024~~EM2025 dataset from 2017~~–~~2021 ~~(Fig. 4a-b~~(-5.1 km in the Beaufort and -0.5 in the Chukchi). Much of the difference in the Beaufort region occurs, between Point Barrow and Kaktovik where our InSAR-derived results show the landfast ice is consistently 6~~–~~10 km narrower. In the Chukchi region, differences between InSAR-derived width and ~~EM2024~~EM2025 monthly mean width occur primarily in Kotzebue Sound. Similar to

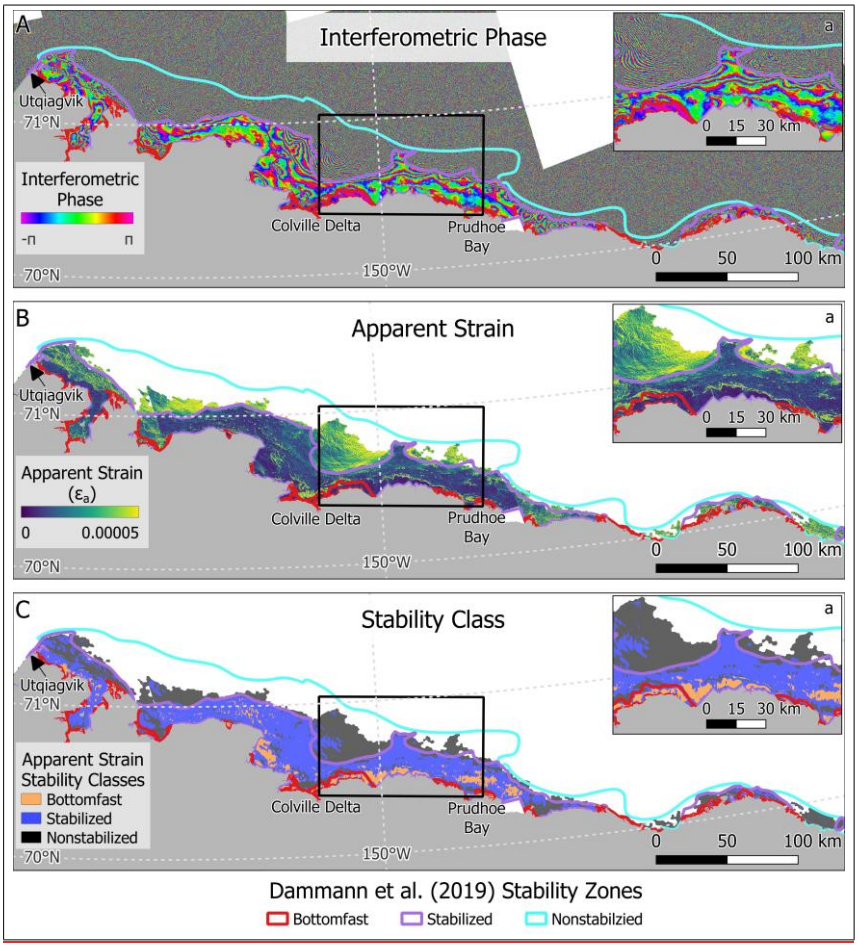


Figure 9. Spatial representation of the interferogram (A), apparent strain (B), and apparent strain derived stability classes (C) compared to the stability zones defined by Dammann et al. (2019) using the same SAR pairs. The black box indicates the location of the inset (a).

the area between Point Barrow and Kaktovik in the Beaufort region, the InSAR-derived width was on average ~~7.7~~8.2 km less than the ~~EM2024~~EM2025 width in Kotzebue Sound during January.

Agreement between InSAR-derived landfast ice extent and the ~~EM2024~~EM2025 dataset is best from February through April. In February ~~and March~~through April, our InSAR-based method still slightly underestimated landfast ice width compared to the ~~EM2024~~EM2025 dataset by an average of 2.~~1~~5 km and ~~1.1~~4.4 km, respectively for the combined Chukchi and Beaufort regions. ~~In April~~ During these months, there are areas where the ~~InSAR-derived~~ coherence based method overestimated the landfast ice ~~width exceeded EM2024 width by an average~~extent. Specifically, during April north of ~~0.7 km across both study regions. The main areas where differences persisted from February through April were Kotzebue Sound and the~~ the Colville Delta~~.~~ (Fig. 3 the coherence-based SLIE is 1-2 km further offshore than the EM2025. This is an area identified as a node (Mahoney et al., 2014) and in proximity to grounded ridges (Lange et al., 2024). Finally, in May, the InSAR based method under measured the landfast ice width consistently across the study region. The consistent under measuring of landfast ice in May is attributed to surface melting causing a loss of coherence between acquisitions. Overall, the ~~InSAR~~ coherence-based identification of landfast ice measures the landfast ice width well however the there are certain areas where the combination of

12 days between acquisitions and C-band SAR prevent the methods from identifying landfast ice. On this basis, we find that 12-day repeat Sentinel-1 InSAR may be a useful tool for helping discriminate landfast ice sea ice extent during the coldest months of the year when the dielectric properties of the ice surface are most stable. With the imminent launch of the NISAR satellite, 12-day L-band InSAR will be possible for all but the most northern regions of landfast ice in the Arctic. Meyer et al. ~~(2011)~~(2011) showed that L-band coherence could be maintained for 45 days over landfast ice and so we anticipate that NISAR may allow us to extend the useful season of InSAR for this landfast ice detection.

## ~~4.2.~~ 4.2 Regional variability and annual evolution of landfast ice stability

We have shown that, over the study area, the distribution of apparent strain evolves such that the modal value of ~~$\epsilon_e$-$\epsilon_a$~~ decreases monotonically from December to May across the whole study region (7. We interpret this to indicate that landfast ice becomes more stable the longer it remains in place over winter. To better understand the processes likely to responsible for this, we partitioned this analysis between the 11 subregions shown in ~~Fig. 1. In most cases~~Figure 1 and calculated the distribution of monthly mean apparent strain in each subregion (Fig 10). Similar to the study region as a whole, the mode of the apparent strain distribution decreases monotonically from month to month, such that landfast ice transitions toward more stable categories over time ~~(Fig. 10).~~in most subregions (Fig. 10). Subregion 9, Point Barrow to Kaktovik (Fig. 10), is the best representation of the evolution of apparent strain in a subregion throughout the year due to the extensive amount of landfast ice and the variety of coastline

types. It should be noted that, from December to April, this increase in stability occurs while the overall extent of landfast ice also increases,

375 suggesting that the process by which the SLIE advances also increases the stability of the ice overall.

In some ~~sub-regions~~subregions, the total landfast ice extent in May in less than that in April, so any increase in the modal ~~$\epsilon_a$~~$\dot{\epsilon}_a$ value between these two months likely indicates that the least stable landfast ice is the first to detach. ~~This is especially apparent in subregion 6 ,Cape Lisburne to Point Hope, where the monthly average $\epsilon_a$ values for May fall almost entirely within the bottomfast and stabilized ice classes (Fig. 10f).~~ However, not all subregions follow a monotonic decrease in apparent strain throughout the season.

~~Despite the overall tendency of $\epsilon_a$ to monotonically decrease over winter, we note that subregions 3, 5, and 7 behaved differently. In subregion 3, Outer Kotzebue Sound, the modal apparent strain decreased until March but remained similar in April. By May, the only landfast ice remaining within Kotzebue Sound was not intersected by any of the coast vectors for this subregion. Subregion 5, Cape Krusenstern to Point Hope, is the only south facing subregion and exhibited increasing apparent strain from December to March, indicating that landfast ice becomes increasingly unstable in this region as it extends from shore. This suggests the landfast ice along this stretch of coast includes relatively few grounded ridges. However, there is a pronounced shift in the $\epsilon_a$ distribution in April toward increased stability, which we cannot explain with the data available. In subregion 7, Cape Lisburne to Wainwright, the lowest modal value of $\epsilon_a$ was observed in December, when the only landfast ice present occurred within lagoons. However, the highest modal values of $\epsilon_a$ in this subregion occurred in January and February as landfast ice began forming outside the lagoons. In March, April, and May, $\epsilon_a$ values decreased monotonically in other regions.~~

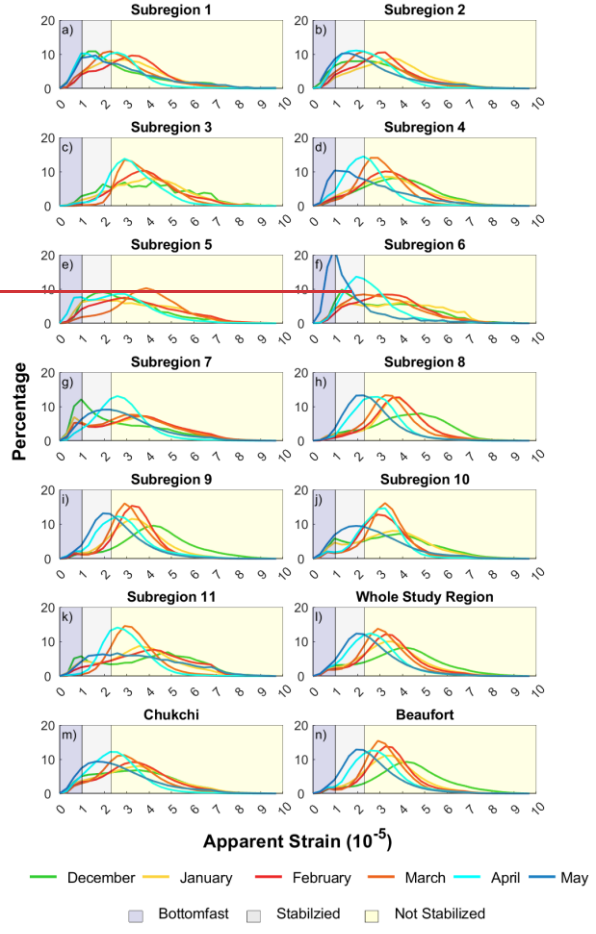
Subregion 1
Subregion 2
Subregion 3
Subregion 4
Subregion 5
Subregion 6
Subregion 7
Subregion 8
Subregion 9
Subregion 10
Subregion 11
Whole Study Region
Chukchi
Beaufort
Percentage
Apparent Strain ($10^{-5}$)
December
January
February
March
April
May
Bottomfast
Stabilzied
Not Stabilized

~~**Figure 10: Monthly distribution of interferometric phase gradient in each of the 2 regions, 11 subregions, and entire study region. Shaded regions indicated the stability classes discussed in section 2.5**~~

Subregions with extensive lagoon systems have different trends of apparent strain distributions throughout the season. Subregion 1 - Northern Chukotka Peninsula, Subregion 2 - Northern Seward Peninsula, and Subregion 7 - Point Hope to Wainwright are regions where the coastline is primarily composed of lagoons. The landfast ice within these lagoons forms prior to landfast

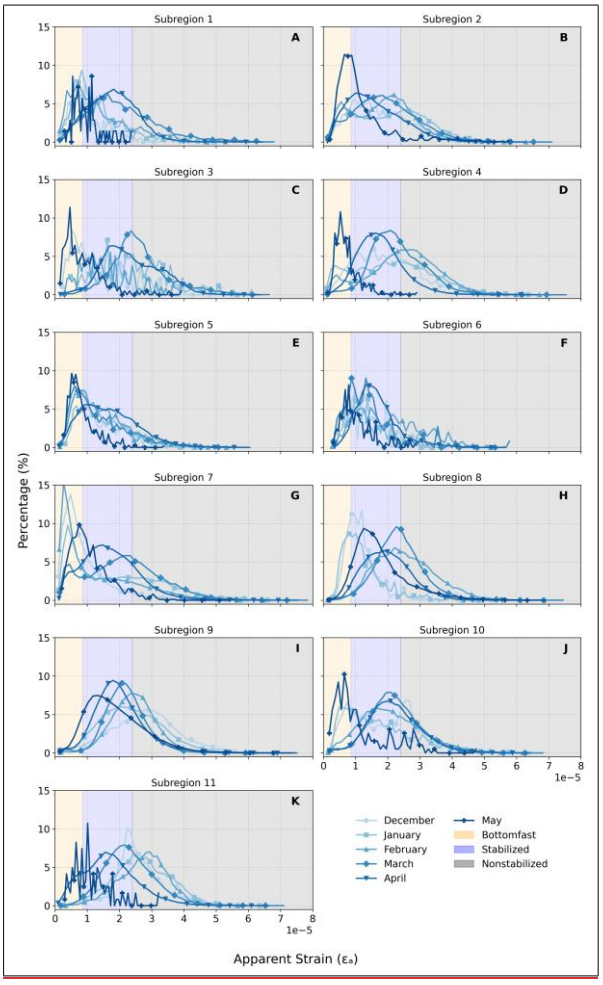
Subregion 1
A
Subregion 2
B
Subregion 3
C
Subregion 4
D
Subregion 5
E
Subregion 6
F
Subregion 7
G
Subregion 8
H
Subregion 9
I
Subregion 10
J
Subregion 11
K
Percentage (%)
Apparent Strain (εₐ)
1e−5
December
January
February
March
April
May
Bottomfast
Stabilized
Nonstabilized

Figure 10. Distributions of monthly apparent strain in the 11 subregions described in Figure 1. Each month form December through May is shown is darker shades of blue as it goes from December to May. Shaded regions indicate the apparent strain values associated with each stability class: orange is bottomfast, blue is stabilized, and gray is nonstabilized

ice outside of the lagoons. During the months when fast ice only exists within a lagoon, the distribution indicated a lower apparent strain mode. In this instance, all the landfast ice is being stabilized by the barrier island, and depending on the depth of the water and the thickness of the ice, it could be bottomfast. The distribution of apparent strain within Subregion 7 (Fig. 10G),is a

385 prime example of the distribution in a subregion dominated by lagoons. The monthly distributions are concentrated within the bottomfast class in the early months (December-February), then follow a typical seasonal progression in March through May (Fig. 10G). The high percentage of low apparent values in subregion 7 during the early months is due to the landfast ice not existing outside of shallow lagoons (Fig 5A-C). It is not until March, when substantial landfast ice exists outside of the shallow lagoons.

## ~~4.3.~~ 390 4.3 Identification of abrupt increases in apparent strain associated with grounded features

We have shown that the three apparent strain thresholds we defined in section ~~3.3~~3.3 for bottomfast, stabilized, and ~~not stabilized~~nonstabilized landfast ice align relatively well with the extent of equivalent stability ~~regions~~zones identified qualitatively by Dammann et al. (2019) from single interferograms. Within other single-interferogram apparent strain maps, we commonly observe strong gradients in apparent strain that are not evident in the monthly average maps illustrated in Figures ~~5~~5 and ~~6~~6 which we believe are associated

395 with ~~bottomfast or~~the transition from grounded to floating landfast ice ~~features~~. For example, at the seaward edge of the bottomfast ice, there ~~is a~~are tide crack ~~zone~~zones where the floating landfast ice flexes in response to sea level variations while the bottomfast ice remains stationary. The difference in vertical motion across this narrow region (typically a few 10s of ~~m~~meters wide) leads to a region of high fringe density, like those found at the grounding lines of ice shelves and tidewater glaciers (Friedl et al., ~~2020),~~2019), resulting in high apparent strain. Examples of such features can be seen in two apparent strain maps from April 05 ~~–~~ 17, 2017 (Fig.~~11a~~11A) and

400 April 09 ~~–~~ 21, 2022 (Fig. ~~11b~~11B) near ~~the shoreline and around barrier islands~~Oliktok Point in the ~~eastern~~ Beaufort region~~, denoted by red boxes. In addition, we observe isolated regions~~. We see abrupt increases of ~~high~~ apparent strain ~~within regions classified as stabilized~~in both maps associated with a tide crack, a barrier island, and a grounded ridge (Fig. 11C). During 2022 the landfast ice ~~(indicated by cyan boxes in Fig. 11b~~was more extensive allowing for the formation of a second grounded ridge (Fig. 11C). The resemblance of these features to those around barrier islands leads us to interpret them as the tide crack zone around grounded ridges. Moreover, they occur at the locations grounded ridges have been identified in this region during the 2021-22 landfast ice season by Lange et al. (2024). In addition,

~~The shoreward most feature identified in 2022 (Fig. 11b) occurred at approximately the same location as the boundary between the stabilized and not stabilized landfast ice in 2017 (marked by the red line in Fig. 11a) and 2022 seasons. This boundary by another steep gradient in apparent strain, but one which differs from those associated with tide cracks in that it represents a step change between regions of comparatively low and high apparent strain. This is illustrated by looking at apparent strain values along the transect line extending due north from near Oliktok Point, Alaska (Fig. 11c, d). This transect starts at the shoreline and in both years shows elevated apparent strain values as it crosses a barrier island before encountering another peak in apparent strain around 12 km from the shore. In 2017, the apparent strain values seaward of this feature elevated in the range of not stabilized ice (Fig. 11c), but in 2022 they remain lower in the range for stabilized ice until approximately 2 km beyond the seaward most grounded feature. At this point we see a step change in apparent strain, similar to that at the location of the shoreward ridge in 2017, that marks the boundary between the stabilized and not stabilized ice classes. Hence, although the boundary between stabilized and not stabilized is not always marked by such a sharp gradient in apparent strain, its position in locations like Oliktok Point appears to be controlled in part by the locations of features that we interpret to be grounded ridges.~~

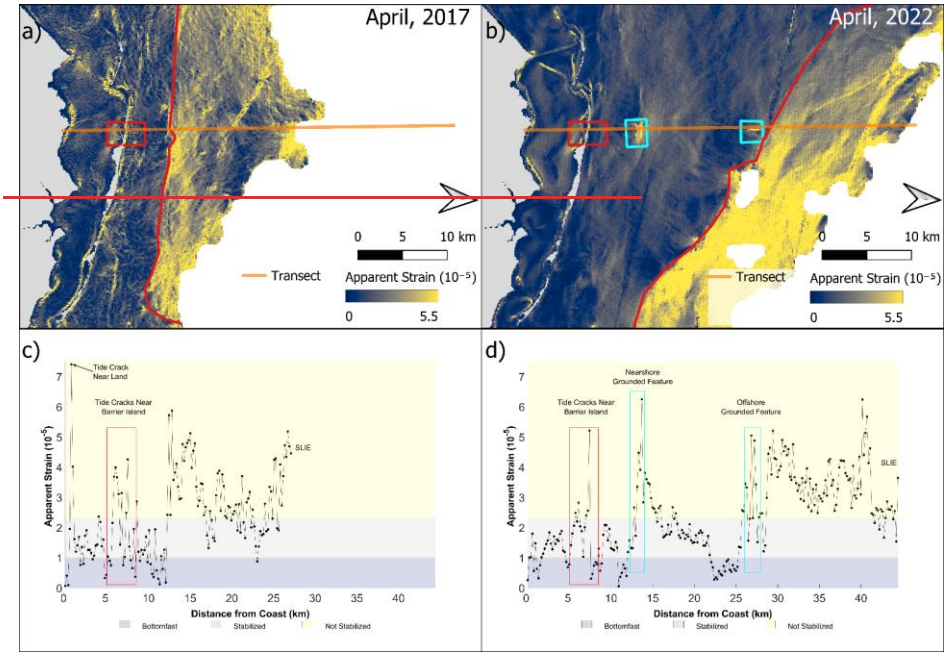


~~**Figure 11: Apparent strain values derived from two single-pair interferograms from a) April 05, 2017 – April 17, 2017, and b) April 09, 2022 – April 21, 2022, near Prudhoe Bay, Alaska. The red boxes indicate high apparent strain values either side of a barrier island areas interpreted to be tide cracks along the transect. The cyan boxes panel b) identify similar features, which we interpret as grounded ridges. The apparent strain values along the transects in panels a) and b) are shown in panels c) and d) respectively.**~~

similar patterns in apparent strain values can be observed on within the lagoon and oceanward of the barrier island, providing further evidence the abrupt gradient in apparent strain is associated with a stabilizing feature.

The shoreward feature identified as a grounded ridge occurred in approximately the same location in both 2017 and 2022, but the apparent strain patten deviates offshore of this location around 23 km. Both transects indicate a reduction of apparent strain offshore of the seaward grounded ridge (Fig. 11C). We believe this to to be the local stabilized affect of a grounded feature. However proving and interpreting this is outside the scope of this study. It is also possible the areas high apparent strain gradients are not the grounded features, but the low apparent strain features about these areas. A direct comparison to the

location of the grounded ridges by Lange et al. (2024) could provide evidence of the apparent strain pattern related to the grounded features versus the fast ice surrounding the ridge.

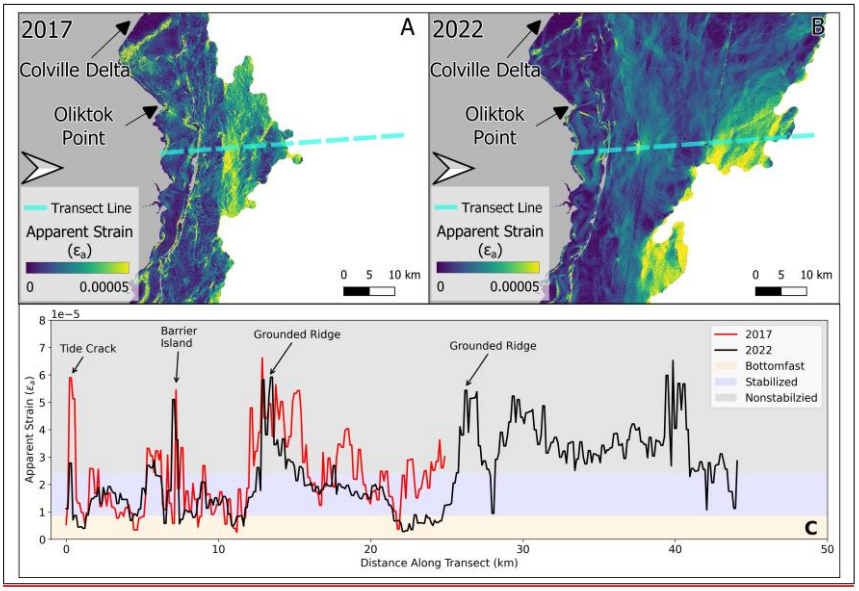


Figure 11. Apparent strain maps from April 2017 (A) and April 2022 (B) and the associated apparent strain values along a transect near Oliktok Point, Alaska (C). Apparent strain values along each transect (2017 red, and 2022 black) can be sorted into stability classes and used to identify the location of features.

## ~~5.~~ 5 Conclusion

InSAR-based methods hold great promise for improving our understanding of both the spatial extent of landfast sea ice and its relative stability. Meyer et al. (2011) already demonstrated the usefulness of interferometric coherence in delineating landfast ice from the mobile pack ice using 45-day repeat L-band PALSAR data. Our investigation shows that ~~the same~~a similar approach ~~works~~with a coherence threshold for C-band can work well during ~~most of~~ the ~~year~~winter months and throughout most of our study area using 12-day

C-band Sentinel-1 data. During the winter months, February ~~–~~- April, landfast ice widths derived from coherence threshold ~~approach~~ap-
proach typically agreed to within a few km, of those derived from the ~~EM2024~~EM2025 dataset (Fig ~~4c-e~~4C-E). However, factors unrelated to the motion of the ice reduce coherence at the beginning and end of the season, occasionally resulting in false absence of landfast ice (corresponding to a 100% underestimate in ~~Fig 4e~~Figure 4E and ~~f~~F, for example). Hence, the usefulness of out interferometric coherence method for identifying landfast ice would be improved with either a shorter period between SAR images or a use of longer radar wavelength. We therefore look forward to the launch of the NASA-ISRO synthetic aperture radar (NISAR)
currently scheduled to launch in 2025. The L-band sensor and 12-day repeat interval should open new opportunities for routine mapping of landfast extent using InSAR.

~~In a quantitative expansion of Dammann et al's (2019) work, we find that apparent strain, $\epsilon_a$,~~In a quantitative expansion the work done by Dammann et al. (2019), we find apparent strain, $\epsilon_a$, can serve as a meaningful measure landfast ice stability. Specifically, we find that the distributions of ~~$\epsilon_a$~~$\epsilon_a$ values within the bottomfast ice zone and either seaward or shoreward of barrier islands have distinct modes. This allows us to define three landfast ice stability classes on
the basis of apparent strain: bottomfast ice ( ~~$\epsilon_a < 1.0 \times 10^{-5}$~~), $\epsilon_a \leq 8.6\times10^{-6}$), stabilized ( ~~$1.0 \times 10^{-5} \leq \epsilon_a < 2.3 \times 10^{-5}$~~), $8.6\times10^{-6} < \epsilon_a \leq 2.4\times10^{-5}$), and ~~not stabilized ($\epsilon_a \geq 2.3 \times 10^{-5}$)~~,nonstabilized ($\epsilon_a > 2.4\times10^{-5}$). Single interferograms indicate a spatially abrupt change in apparent strain between the stabilized and ~~not stabilized~~nonstabilized landfast ice. These abrupt changes are not present within the monthly average apparent strain images (~~Figs. 5~~Fig. 5 and ~~6) which suggests they do not commonly 6~~). The grounded ridges likely persist between interferograms~~. This is likely because~~ in the same season. However, they are not present in the monthly averages indicating the the strain field in landfast ice evolves more rapidly than the repeat interval of Sentinel-1 and because
the monthly averages combine results from different viewing geometries. Nonetheless, the boundary between stabilized and not stabilized ice is often associated with features that we interpret to be grounded features (Fig. ~~11),~~11), which suggests our classification represents physical difference in the strain experienced by landfast ice on either side. To our knowledge, this is the first time InSAR has been used to identify individual grounded ridges based on localized values of high apparent strain ~~or phase gradient.~~ .

Our interpretation on this matter is strongly supported by matching the locations of grounded ridges identified by Lange et al. (2024~~),~~), based on ICESat-2 altimetry data. Moreover, our observations support their findings that grounded ridges are commonly located shoreward of the landfast ice edge.

Along with the establishment of the apparent strain thresholds we defined, we observed a decrease in apparent strain throughout the season. The increase in stability the longer the landfast ice is likely due to thickening, but further investigation into the cause is needed. A fundamental flaw in using information derived from interferometry is the inability of InSAR to capture

along-track deformation. Being limited to the magnitude of line-of-sight deformation causes an ~~underrepresentation~~under representation of the total possible deformation which occurred. Implementing methods to resolve the two-dimensional strain, demonstrated by Fedders et al. (2024)~~,~~ would improve our ability to classify landfast ice stability based on the apparent strain. The ability of InSAR to identify these areas of varying stability can hold immense value to members of Arctic coastal communities such that they can continue to operate on the landfast ice safely.

## ~~6. Code Availability~~

*availability.* Code for processing of the ASF Vertex outputs into apparent strain can be found here ~~(https://github.com/aheinhorn/Alaska_InSAR_CODE).~~(https://github.com/aheinhorn/ Alaska_InSAR_CODE). All the code for analyzing the fast ice extent of the ~~InSAR~~coherence derived width and ~~EM2024~~EM2025 derived width can be found here ~~(https://github.com/armahoney/SLIEalyzer)~~(https://github.com/armahoney/SLIEalyzer)

## ~~7. Data Availability~~

*availability.* Sentinel-1 SAR imagery are openly accessible at the Alaska Satellite Facility's Vertex tool ~~(https://search.asf.alaska.edu),~~(https://search.asf.alaska.edu), where users can search for imagery, request on-demand processing (include InSAR products), and download data. Registration with NASA EarthData is required but is open to anyone. The ~~EM2024~~EM2025 dataset is available through the University of Alaska Fairbanks Scenarios Network for Alaska and Arctic Planning (SNAP) at ~~http://data.snap.uaf.edu/data/Base/Other/Landfast_Sea_Ice/Chukchi_Daily (for the Chukchi region) and http://data.snap.uaf.edu/data/Base/Other/Landfast_Sea_Ice/Beaufort_Daily~~ https://catalog.snap.uaf.edu/geonetwork/srv/eng/catalog.search#/metadata/a6323019-0023-4e0d-98dc-a01b13b the Chukchi region) and https://catalog.snap.uaf.edu/geonetwork/srv/eng/catalog.search#/metadata/5adee563-786d-4b54-bbec-56dea055ec9a (for the Beaufort region) under a Creative Commons license (CC-BY 4.0)

## ~~8. Author Contribution~~

*contributions.* All authors edited the manuscript. AHE led the analysis, produced ~~all figured except Fig. 1~~figures, and drafted the ~~paper~~article. ARM ~~produced Fig. 1~~created the 460 SLIEalizer package and provided scientific and editorial feedback and direction to the project.

## 9. Competing Interests

interests. The authors declare that they have no conflict of interest.

## 10. Disclaimer

. The views and conclusions contained on the website are those of the authors and should not be interpreted as representing the opinions or policies of the US Government, nor does mention of trade names or commercial products constitute endorsement or recommendation for use.

## 11. Acknowledgments

465 *Acknowledgements.* Study collaboration and funding were provided by the US Department of the Interior, Bureau of Ocean Energy Management (BOEM), Environmental Studies Program, Washington, DC, under Agreement Number M19AC00021. We are also extremely grateful to the members of our Science Review Board, Hajo Eicken, Andrew Roberts, and John Walsh

## 12. Financial Support

Study collaboration and funding were provided by the US Department of the Interior, Bureau of Ocean Energy Management (BOEM), Environmental Studies Program, Washington, DC, under Agreement Number M19AC00021

# Appendix A: Supplementary

## A1 Coherence Threshold Derivation

Derivation of the C-Band coherence threshold to delineate landfast ice from mobile pack ice was done using SAR pairs acquired in both the Chukchi and Beaufort regions, throughout the winter to ensure the threshold was applicable to all SAR pairs used in this study. Landfast ice has been identified using a simple coherence threshold (Meyer et al., 2011). However, due to the increased sensitivity and resulting reduction of coherence associated with a shorter wavelength, the 0.1 threshold established by Meyer et al. (2011) using L-Band is not applicable to SAR pairs acquired using a C-Band SAR. Thus we needed to establish a coherence threshold to identify landfast ice using C-Band. We selected 2 reference scenes, one from the Chukchi region and one from the Beaufort and SAR pairs occurring in each month from December through June. The Chukchi reference scene is located on the north coast of the Seward Peninsula, covering most of the area denoted as Subregion 2 in Figure 1. The Beaufort reference scene is located about Barrow Alaska and primarily located in Subregion 9 (Fig. 1). While both primary and secondary acquisitions do not always occur in the month assigned, these were the SAR pairs available which fit our spatial and temporal baseline criteria, detailed in Section 2.3. Details about the SAR pairs used for each month can be found in A1. We used each normalized coherence image produced by the HyP3 processing Hogenson et al. (2016) to derived the best coherence threshold for landfast ice using C-band.

Delineating landfast ice from mobile pack ice can be accomplished by applying a threshold to the coherence image, then applying morphological filtering to remove spurious offshore areas being identified as landfast ice. Prior to the testing of different coherence thresholds we computed the monthly minimum landfast ice extent in each month for the 2017-2018 season using the EM2025 dataset to represent the true fast ice extent. The minium landfast ice extent was chosen as coherence is only maintained if the landfast ice does not breakout over the entire 12-day orbit. In addition, new landfast ice formed between the acquisition dates would not present as coherent. Thus we found it appropriate to use the monthly minimum landfast ice extent measured by the EM2025 dataset as a comparison. The pixels shoreward of the monthly minimum landfast ice extent were treated as fast ice, and pixels outside were treated as not landfast ice. To maintain consistent window sizes with the phase gradient calculation, Section 2.4 we applied a 4 pixel smoothing filter to the coherence images. An example of a normalized coherence image can be seen in Figure A1. The SAR pair is the same used in A3H. The pixels from each normalize coherence images were then sorted into areas identified as landfast ice or not landfast ice by the EM2025 monthly minimum. The distribution of normalized coherence values for areas identified as landfast ice (solid) and not landfast ice (dashed) in the corresponding month can be seen in Figure A2. In both regions, the areas identified as not fast ice peak around 0.2. This is in contrast to the areas identified as landfast ice which are more evenly distributed across higher coherence values or having

peaks above 0.8. In the Chukchi (December, January, and June) and Beaufort (June), the distribution of coherence is similar to
the not landfast ice areas (Fig. A2A/B). We suspect the reduction in coherence in the early months is due to inherent bias when using active microwave remote sensing over growing sea ice while in June we suspect surface melting to cause the coherence distribution to be similar to not landfast ice. Figure A2 confirms the coherence threshold for established by Meyer et al. (2011) of 0.1 using L-Band is not directly transferable to C-band.

To derive the C-Band coherence threshold for identifying landfast ice, we used a systematic approach by applying different thresholds from 0.01 to 1, increasing in 0.01 increments, and computing a confusion matrix for each month. The categories of the confusion matrices were: Correct landfast ice (EM2025 landfast ice, coherence landfast ice), actually landfast ice but predicted not landfast ice (EM2025 landfast ice, coherence not landfast ice), not landfast ice but predicted landfast ice (EM2025 not landfast ice, coherence landfast ice), and correct not landfast ice (EM2025 not landfast ice, coherence not landfast ice). We then calculated the threshold with the highest percentage of correctly identified landfast ice pixels and correctly identified not
landfast ice pixel for each month in each sector. However, due to a high percentage of the pixels being classed as not fast ice, we found the best thresholds identified had higher thresholds as this method favored true negatives more than true positives. To account for the imbalance in true negatives and true positives we weighted the accuracy of each threshold. Then we used the weighted accuracies determined the best coherence threshold in each sector and month, summarized in (Table A2). Based on the distribution of these best thresholds for each month and the previous knowledge there are SAR pairs which struggled to
retain coherence due to suspected thin ice and melting, Chukchi (December, January, and June) and Beaufort (June) we chose 0.3 as the coherence threshold to identify landfast ice with C-Band.

The 0.3 coherence threshold was then applied to the 14 SAR pairs A1 to confirm the coherence method captured the spatial pattern of landfast ice in the Chukchi and Beaufort regions. Similar to the derivation of the threshold we compared the spatial extent of the landfast ice identified by the coherence method to the minimum extent measured by the associated month during
the 2017-2018 season from the EM2025 dataset. Areas which both methods identified landfast ice colored green, false positives are dark orange, false negatives are light orange, and cyan areas are areas both methods identified as not landfast ice (Fig. A3). In both regions, the coherence method over estimates the monthly fast ice minimum extent and under estimates in the latter half, expectantly in the Beaufort region. We included the monthly maximum extent, denoted by the black line in each panel of
Figure A3 as a way to show the range of landfast ice extent during each month since the minimum landfast ice might not have

occurred between SAR acquisitions. During June in the Beaufort region (Fig. A3N) the coherence method identified no fast ice. This is due to surface melting confirmed by the presence of melt pond from MODIS imagery.

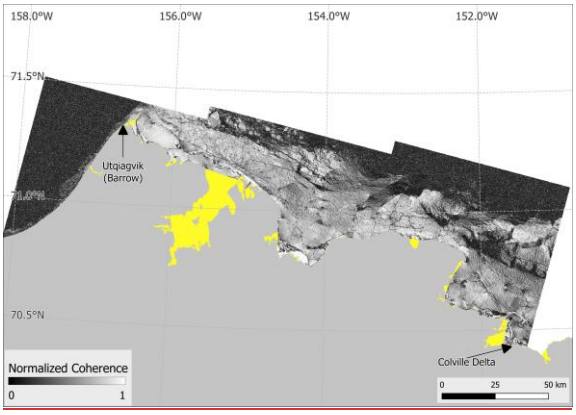


Figure A1. Example of a normalize coherence image from SAR pairs March 11th, 2018 and March 23rd, 2018. Black indicates low coherence while white indicates high coherence. Yellow regions are shadow regions.

| Primary Acquisition Date | Secondary Acquisition Date | Region | Month Assigned |
|---|---|---|---|
| December 13th, 2017 | December 25th, 2017 | Chukchi | December |
| January 18th, 2018 | January 30th, 2018 | | January |
| February 11th, 2018 | February 23rd, 2018 | | February |
| March 31st, 2018 | April 12th, 2018 | | March |
| April 12th, 2018 | April 24th, 2018 | | April |
| May 18th, 2018 | May 30th, 2018 | | May |
| June 11th, 2018 | June 23rd, 2018 | | June |
| December 17th, 2017 | December 29th, 2017 | Beaufort | December |
| January 22nd, 2018 | February 3rd, 2018 | | January |
| February 3rd, 2018 | February 15th, 2018 | | February |

| | | | |
|---|---|---|---|
| March 11th, 2018 | March 23rd, 2018 | | March |
| April 4th, 2018 | April 16th, 2018 | | April |
| April 28th, 2018 | May 10th, 2018 | | May |
| June 3rd, 2018 | June 15th, 2018 | | June |

Table A1. Acquisition dates of Sentinel-1 SAR pairs used for the derivation the the coherence threshold

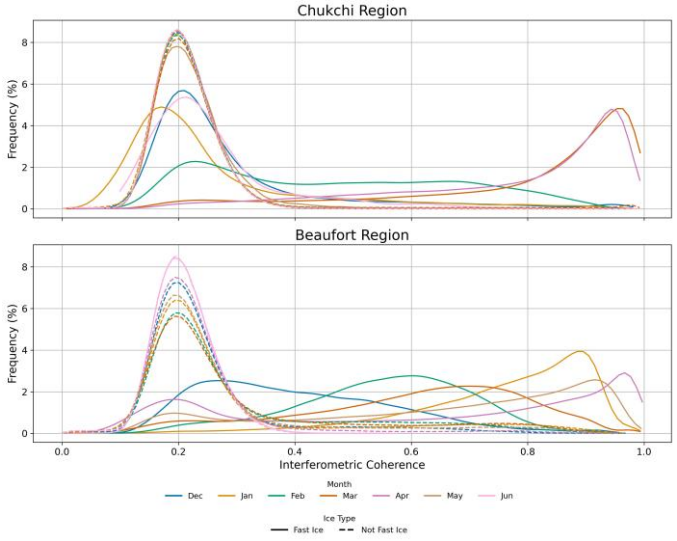


Figure A2. The distribution of normalized coherence values from SAR pairs acquired during each month from December through June of the 2017-2018 landfast ice season in the Chukchi and Beaufort regions. Monthly coherence distributions: solid lines show areas identified as landfast ice by EM2025, dashed lines show areas not identified as landfast ice.

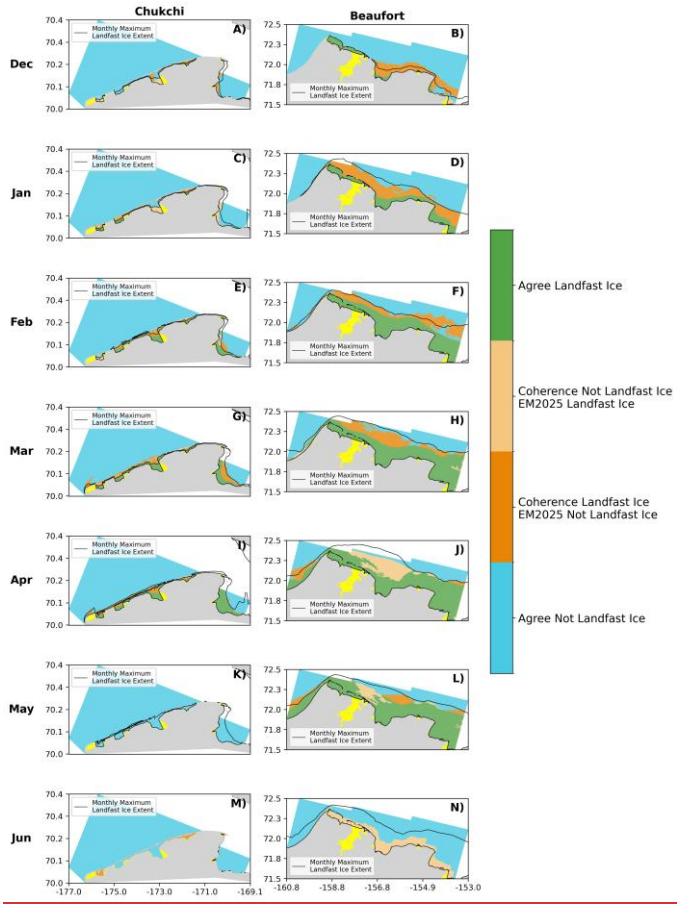


Figure A3. Spatial representation of the confusion matrix comparing the identification of landfast ice for each month and sector when using a 0.3 coherence threshold and monthly minimum extent from the EM2025 dataset during the 2017-2018 season. Yellow regions are shadow regions (Section 2.2)

| Month | Region | Threshold | Percentage Correct (%) |
|---|---|---|---|
| December | Chukchi | 0.27 | 58 |
| January | | 0.31 | 60 |
| February | | 0.30 | 81 |
| March | | 0.35 | 92 |
| April | | 0.35 | 96 |
| May | | 0.30 | 60 |
| June | | 0.26 | 59 |
| December | Beaufort | 0.29 | 77 |
| January | | 0.50 | 86 |
| February | | 0.35 | 83 |
| March | | 0.37 | 80 |
| April | | 0.35 | 80 |
| May | | 0.36 | 84 |
| June | | 0.17 | 51 |

Table A2. Best coherence threshold identified in each month and sector. And the percentage of pixels which the coherence method agreed with the EM2025 classification.

## ~~13.~~ References


~~Barry, R. G., Moritz, R. E., & Rogers, J. C. (1979). The fast ice regimes of the Beaufort and Chukchi Sea coasts, Alaska. *Cold Regions Science and Technology*, *1*(2). https://doi.org/10.1016/0165-232X(79)90006-5~~

~~Bieniek PA, Eicken H, Jin M, Mahoney AR, Jones J, Bhatt US. 2022. Seasonal forecasting of landfast ice in Foggy Island Bay, Alaska in support of ice road operations. *Cold Regions Science and Technology*. 201:103618 doi: https://doi.org/10.1016/j.coldregions.2022.103618.~~

~~Cooley SW, Ryan JC. 2024. Community-scale changes to landfast ice along the coast of Alaska over 2000-2022. *Environmental Research Letters*. 19(2):024013 doi: 10.1088/1748-9326/ad1c7b~~

~~Dammann DO, Eicken H, Meyer FJ, Mahoney AR. 2016. Assessing small-scale deformation and stability of landfast sea ice on seasonal timescales through L-band SAR interferometry and inverse modeling. *Remote Sensing of Environment*. 187:492-504 doi: http://dx.doi.org/10.1016/j.rse.2016.10.032.~~

Dammann DO, Eriksson LEB, Mahoney AR, Eicken H, Meyer FJ. 2018. Landfast sea ice stability – mapping pan-Arctic ice regimes with implications for ice use, subsea permafrost and marine habitats. *The Cryosphere Discuss*. 2018:1-23 doi: 10.5194/tc-2018-129.

Dammann, D. O., Eriksson, L. E. B., Mahoney, A. R., Eicken, H., & Meyer, F. J. (2019). Mapping pan-Arctic landfast sea ice stability using Sentinel-1 interferometry. *Cryosphere*, *13*(2), 557–577. https://doi.org/10.5194/tc-13-557-2019

Danielson, S., Johnson, M., Solomon, S., & Perrie, W. (2008). 1-km Gridded Bathymetric Database Based on Ship Soundings: A research tool for the waters of eastern Russia, Alaska & western Canada. *Poster Presentation at the 2008 Alaska Marine Science Symposium*.

Fedders, E., Mahoney, A., Dammann, D. O., Polashenski, C., & Hutchings, J. (2024). Two-dimensional thermal and dynamical strain in landfast sea ice from InSAR: results from a new analytical inverse method and field observations. *Annals of Glaciology*.

Fraser AD, Massom RA, Handcock MS, Reid P, Ohshima KI, Raphael MN, Cartwright J, Klekociuk AR, Wang Z, Porter-Smith R. 2021. Eighteen-year record of circum-Antarctic landfast sea-ice distribution allows detailed baseline characterisation and reveals trends and variability. *The Cryosphere*. 15(11):5061-5077 doi: 10.5194/tc-15-5061-2021.

Fraser AD, Massom RA, Michael KJ. 2009. A Method for Compositing Polar MODIS Satellite Images to Remove Cloud Cover for Landfast Sea-Ice Detection. *IEEE Transactions on Geoscience and Remote Sensing*. 47(9):3272-3282 doi: 10.1109/TGRS.2009.2019726.

Fraser AD, Massom RA, Michael KJ, Galton-Fenzi BK, Lieser JL. 2012. East Antarctic Landfast Sea Ice Distribution and Variability, 2000–08. *Journal of Climate*. 25(4):1137-1156 doi: 10.1175/jcli-d-10-05032.1.

Friedl, P., Weiser, F., Fluhrer, A., & Braun, M. H. (2020). Remote Sensing of Glacier and Ice Sheet Grounding Lines: A Review. 201 *Earth Science Reviews*. https://doi.org/10.1016/j.earscirev.2019.102948

George JC, Huntington HP, Brewster K, Eicken H, Norton DW, Glenn R. 2004. Observations on Shorefast Ice Dynamics in Arctic Alaska and the Responses of the Iñupiat Hunting Community. *Arctic*. 57(4):363-374 doi,

Hogenson, K., Arko, S., Buechler, B., Hogenson, R., Herrmann, J., & Geiger, A. (2016). Hybrid Pluggable Processing Pipeline (HyP3): A cloud-based infrastructure for generic processing of SAR data. *AGU Fall Meeting*.

Hošeková L, Eidam E, Panteleev G, Rainville L, Rogers WE, Thomson J. 2021. Landfast Ice and Coastal Wave Exposure in Northern Alaska. *Geophysical Research Letters*. 48(22):e2021GL095103 doi: https://doi.org/10.1029/2021GL095103.

Itkin P, Losch M, Gerdes R. 2015. Landfast ice affects the stability of the Arctic halocline: Evidence from a numerical model. *Journal of Geophysical Research*: Oceans. 120(4):2622-2635 doi: 10.1002/2014JC010353.

Laidler GJ, Ford JD, Gough WA, Ikummaq T, Gagnon AS, Kowal S, Qrunnut K, Irngaut C. 2009. Travelling and hunting in a changing Arctic: assessing Inuit vulnerability to sea ice change in Igloolik, Nunavut. *Climatic Change*. 94(3-4):363-397 doi: 10.1007/s10584-008-9512-z.

Laidre KL, Stern H, Kovacs KM, Lowry L, Moore SE, Regehr EV, Ferguson SH, Wiig Ø, Boveng P, Angliss RP, Born EW, Litovka D, Quakenbush L, Lydersen C, Vongraven D, Ugarte F. 2015. Arctic marine mammal population status, sea ice habitat loss, and conservation recommendations for the 21st century. *Conservation Biology*. 29(3):724-737 doi: 10.1111/cobi.12474.

Lange, K. A., Bradley, A. C., Duncan, K., Farrell, S. L., & Bradley, A. (2024). Grounded ridge detection and characterization along the Alaskan Arctic coastline using ICESat-2 surface height retrievals. *EGUsphere [Preprint]*. https://doi.org/10.5194/egusphere-2024-1885

Libert, L., Wuite, J., & Nagler, T. (2022). Automatic delineation of cracks with Sentinel-1 interferometry for monitoring ice shelf damage and calving. *Cryosphere*, *16*(4), 1523–1542. https://doi.org/10.5194/tc-16-1523-2022

Lovvorn JR, Rocha AR, Mahoney AH, Jewett SC. 2018. Sustaining ecological and subsistence functions in conservation areas: eider habitat and access by Native hunters along landfast ice. *Environmental Conservation*. 10.1017/S0376892918000103:1-9 doi: 10.1017/S0376892918000103.

Mahoney A, Eicken H, Shapiro L, Graves A. Year. Dempsey JP, editor. Defining and locating the seaward landfast ice edge in northern Alaska. *18th International Conference on Port and Ocean Engineering under Arctic Conditions (POAC '05)*; 2006; Potsdam, N.Y. 991-1001.

Mahoney AR, Bieniek P, Danielson S, Einhorn AH, Hedstrom KS, Jones JM, Klenz T (University of Alaska, Fairbanks, AK). 2024. Landfast ice climatology within the Arctic OCS. Anchorage (*AK*): *U.S. Department of the Interior, Bureau of Ocean Energy Management*. 121 p. Report No.: OCS Study BOEM 2024-034. https://espis.boem.gov/Final%20Reports/BOEM_2024-034.pdf.

Mahoney AR, Eicken H, Gaylord AG, Gens R. 2014. Landfast sea ice extent in the Chukchi and Beaufort Seas: The annual cycle and decadal variability. *Cold Regions Science and Technology*. 103(0):41-56 doi: http://dx.doi.org/10.1016/j.coldregions.2014.03.002.

Mahoney AR, Eicken H, Gaylord AG, Shapiro L. 2007. Alaska landfast sea ice: Links with bathymetry and atmospheric circulation. *Journal of Geophysical Research-Oceans*. 112(C02001) doi: C02001 doi 10.1029/2006jc003559.

Mahoney AR, Turner KE, Hauser DDW, Laxague NJM, Lindsay JM, Whiting AV, Witte CR, Goodwin J, Harris C, Schaeffer RJ, Schaeffer R, Betcher S, Subramaniam A, Zappa CJ. 2021. Thin ice, deep snow and surface flooding in Kotzebue Sound: landfast ice mass balance during two anomalously warm winters and implications for marine mammals and subsistence hunting. *Journal of Glaciology*. 10.1017/jog.2021.49:1-15 doi: 10.1017/jog.2021.49.

Masterson DM. 2009. State-of-the-art of ice-bearing capacity and ice construction. *Cold Regions Science & Technology*. 58(3):99-112 doi: 10.1016/j.coldregions.2009.04.002.

Meyer FJ, Mahoney AR, Eicken H, Denny CL, Druckenmiller HC, Hendricks S. 2011. Mapping arctic landfast ice extent using L-band synthetic aperture radar interferometry. *Remote Sensing of Environment*. 115(12):3029-3043 doi, http://www.sciencedirect.com/science/article/pii/S0034425711002306

Moreira A, Prats-Iraola P, Younis M, Krieger G, Hajnsek I, Papathanassiou KP. 2013. A tutorial on synthetic aperture radar. *IEEE Geoscience and Remote Sensing Magazine*. 1(1):6-43 doi: 10.1109/MGRS.2013.2248301.

Pratt JW. 2022. Mapping Bottomfast Sea Ice in Arctic Lagoons Using Sentinel-1 Interferometery [M.S.]. [http://hdl.handle.net/11122/13090]: University of Alaska Fairbanks.

Winebrenner DP, Holt B, Nelson ED. 1996. Observation of autumn freeze-up in the Beaufort and Chukchi Seas using the ERS-1 synthetic aperture radar. *J Geophys Res*. 101(C7):16401-16419 doi,

World Meteorological Organization. 2024. Sea-ice Information and Services. WMO Geneva.23 p. https://library.wmo.int/idurl/4/31442

Bamler, R. and Hartl, P.: Synthetic aperture radar interferometry, Tech. rep., 1998.

Barry, R. G., Moritz, R. E., and Rogers, J. C.: The fast ice regimes of the Beaufort and Chukchi Sea coasts, Alaska, Cold Regions Science and Technology, 1, https://doi.org/10.1016/0165-232X(79)90006-5, 1979.

Bieniek, P. A., Eicken, H., Jin, M., Mahoney, A. R., Jones, J., and Bhatt, U. S.: Seasonal forecasting of landfast ice in Foggy Island Bay, Alaska in support of ice road operations, Cold Regions Science and Technology, 201, https://doi.org/10.1016/j.coldregions.2022.103618, 2022.

Cooley, S. W. and Ryan, J. C.: Community-scale changes to landfast ice along the coast of Alaska over 2000-2022, Environmental Research Letters, 19, https://doi.org/10.1088/1748-9326/ad1c7b, 2024.

Dammann, D. O., Eicken, H., Meyer, F. J., and Mahoney, A. R.: Assessing small-scale deformation and stability of landfast sea ice on seasonal timescales through L-band SAR interferometry and inverse modeling, Remote Sensing of Environment, 187, 492–504, https://doi.org/10.1016/j.rse.2016.10.032, 2016.

Dammann, D. O., Eicken, H., Mahoney, A. R., Meyer, F. J., Freymueller, J. T., and Kaufman, A. M.: Evaluating landfast sea ice stress and fracture in support of operations on sea ice using SAR interferometry, Cold Regions Science and Technology, 149, 51–64, https://doi.org/10.1016/j.coldregions.2018.02.001, 2018a.

Dammann, D. O., Eriksson, L. E. B., Mahoney, A. R., Stevens, C. W., van der Sanden, J., Eicken, H., Meyer, F. J., and Tweedie, C. E.: Mapping Arctic Bottomfast Sea Ice Using SAR Interferometry, Remote Sensing, 10, https://doi.org/10.3390/rs10050720, 2018b.

Dammann, D. O., Eriksson, L. E. B., Mahoney, A. R., Eicken, H., and Meyer, F. J.: Mapping pan-Arctic landfast sea ice stability using Sentinel-1 interferometry, Cryosphere, 13, 557–577, https://doi.org/10.5194/tc-13-557-2019, 2019.

Dammert, P. B., Leppäranta, M., and Askne, J.: SAR interferometry over baltic sea ice, International Journal of Remote Sensing, 19, 3019–3037, https://doi.org/10.1080/014311698214163, 1998.

Danielson, S. L., Dobbins, E. L., Jakobsson, M., Johnson, M. A., Weingartner, T. J., Williams, W. J., and Zarayskaya, Y.: Sounding the Northern Seas, EOS, 96, https://eos.org/science-updates/sounding-northern-seas, 2015.

Fedders, E., Mahoney, A., Dammann, D. O., Polashenski, C., and Hutchings, J.: Two-dimensional thermal and dynamical strain in landfast sea ice from InSAR: results from a new analytical inverse method and field observations, Annals of Glaciology, 65, 1–14, https://doi.org/https://doi.org/10.1017/aog.2024.29, 2024.

Ferretti, A., Monti-Gaurnieri, A., Prati, C., and Rocca, F.: InSAR Principles: Guidelines for SAR Interf erometry Processing and Interpretation, vol. TM-19, ESA Publications, 2007.

Fraser, A. D., Massom, R. A., Michael, K. J., Galton-Fenzi, B. K., and Lieser, J. L.: East antarctic landfast sea ice distribution and variability, 2000-08, Journal of Climate, 25, 1137–1156, https://doi.org/10.1175/JCLI-D-10-05032.1, 2012.

Fraser, A. D., Massom, R. A., Ohshima, K. I., Willmes, S., Kappes, P. J., Cartwright, J., and Porter-Smith, R.: High-resolution mapping of circum-Antarctic landfast sea ice distribution, 2000-2018, Earth System Science Data, 12, 2987–2999, https://doi.org/10.5194/essd-122987-2020, 2020.

Fraser, A. D., Massom, R. A., Handcock, M. S., Reid, P., Ohshima, K. I., Raphael, M. N., Cartwright, J., Klekociuk, A. R., Wang, Z.,

and Porter-Smith, R.: Eighteen-year record of circum-Antarctic landfast-sea-ice distribution allows detailed baseline characterisation and reveals trends and variability, Cryosphere, 15, 5061–5077, https://doi.org/10.5194/tc-15-5061-2021, 2021.

Friedl, P., Weiser, F., Fluhrer, A., and Braun, M. H.: Remote Sensing of Glacier and Ice Sheet Grounding Lines: A Review 2, 2019.

George, J. C., Zeh, J., Suydam, R., and Clark, C.: Abundance and population trend (1978-2001) of western arctic bowhead whales surveyed near Barrow, Alaska, https://doi.org/10.1111/j.1748-7692.2004.tb01191.x, 2004.

Hogenson, K., Arko, S., Buechler, B., Hogenson, R., Herrmann, J., and Geiger, A.: Hybrid Pluggable Processing Pipeline (HyP3): A cloudbased infrastructure for generic processing of SAR data, in: AGU Fall Meeting, 2016.

Hošeková, L., Eidam, E., Panteleev, G., Rainville, L., Rogers, W. E., and Thomson, J.: Landfast Ice and Coastal Wave Exposure in Northern Alaska, Geophysical Research Letters, 48, https://doi.org/10.1029/2021GL095103, 2021.

Itkin, P., Losch, M., and Gerdes, R.: Landfast ice affects the stability of the Arctic halocline: Evidence from a numerical model, Journal of Geophysical Research: Oceans, 120, 2622–2635, https://doi.org/10.1002/2014JC010353, 2015.

Laidre, K. L., Stirling, I., Lowry, L. F., Wiig, , Heide-Jørgensen, M. P., and Ferguson, S. H.: QUANTIFYING THE SENSITIVITY OF ARCTIC MARINE MAMMALS TO CLIMATE-INDUCED HABITAT CHANGE, 2008.

Laidre, K. L., Stern, H., Kovacs, K. M., Lowry, L., Moore, S. E., Regehr, E. V., Ferguson, S. H., Wiig, , Boveng, P., Angliss, R. P., Born, E. W., Litovka, D., Quakenbush, L., Lydersen, C., Vongraven, D., and Ugarte, F.: Arctic marine mammal population status, sea ice habitat loss, and conservation recommendations for the 21st century, Conservation Biology, 29, 724–737, https://doi.org/10.1111/cobi.12474, 2015.

Lange, K. A., Bradley, A. C., Duncan, K., Farrell, S. L., and Bradley, A.: Grounded ridge detection and characterization along the Alaskan Arctic coastline using ICESat-2 surface height retrievals, EGUsphere [preprint], https://doi.org/10.5194/egusphere-2024-1885, 2024.

Li, S., Shapiro, L., Mcnutt, L., and Jeffers, A.: Application of Satellite Radar Interferometry to the Detection of Sea Ice Deformation, Journal of the Remote Sensing Society of Japan, 16, 153–163, 1996.

Libert, L., Wuite, J., and Nagler, T.: Automatic delineation of cracks with Sentinel-1 interferometry for monitoring ice shelf damage and calving, Cryosphere, 16, 1523–1542, https://doi.org/10.5194/tc-16-1523-2022, 2022.

Lovvorn, J. R., Anderson, E. M., Rocha, A. R., Larned, W. W., Grebmeier, J. M., Cooper, L. W., Kolts, J. M., and North, C. A.: Variable wind, pack ice, and prey dispersion affect the long-term adequacy of protected areas for an Arctic sea duck, Ecological Applications, 24, 396–412, https://doi.org/10.1890/13-0411.1, 2014.

Mahoney, A., Eicken, H., Graves, A., and Shapiro, L.: DEFINING AND LOCATING THE SEAWARD LANDFAST ICE EDGE IN NORTHERN ALASKA, Int. Conf. on Port and Ocean Eng. Under Arctic Conditions, 3, 991–1000, 2006.

Mahoney, A., Eicken, H., Gaylord, A. G., and Shapiro, L.: Alaska landfast sea ice: Links with bathymetry and atmospheric circulation, Journal of Geophysical Research: Oceans, 112, https://doi.org/10.1029/2006JC003559, 2007.

Mahoney, A., Bieniek, P., Danielson, S., Einhorn, A., Hedstrom, K., Jones, J., and Klenz, T.: Landfast Ice Climatology within the Arctic OCS, 2024.

Mahoney, A. R. and Einhorn, A. H.: The Evolving Decline of Landfast Sea Ice in Northern Alaska and Adjacent Waters: Results from an Updated Climatology, Journal of Geophysical Research - Oceans, In Review, https://doi.org/10.22541/essoar.173939541.17906910/v1, 2025.

Mahoney, A. R., Eicken, H., Gaylord, A. G., and Gens, R.: Landfast sea ice extent in the Chukchi and Beaufort Seas: The annual cycle and decadal variability, Cold Regions Science and Technology, 103, 41–56, https://doi.org/10.1016/j.coldregions.2014.03.003, 2014.

Mahoney, A. R., Turner, K. E., Hauser, D. D. W., Laxague, N. J. M., Lindsay, J. M., Whiting, A. V., Witte, C. R., Goodwin, J., Harris, C., Schaeffer, R. J., Schaeffer, R., Betcher, S., Subramaniam, A., and Zappa, C. J.: Thin ice, deep snow and surface flooding in Kotzebue Sound: Landfast ice mass balance during two anomalously warm winters and implications for marine mammals and subsistence hunting, Journal of Glaciology, 67, 1013–1027, https://doi.org/10.1017/jog.2021.49, 2021.

Masterson, D. M.: State of the art of ice bearing capacity and ice construction, Cold Regions Science and Technology, 58, 99–112, https://doi.org/10.1016/j.coldregions.2009.04.002, 2009.

Meyer, F. J., Mahoney, A. R., Eicken, H., Denny, C. L., Druckenmiller, H. C., and Hendricks, S.: Mapping arctic landfast ice extent using L-band synthetic aperture radar interferometry, Remote Sensing of Environment, 115, 3029–3043, https://doi.org/10.1016/j.rse.2011.06.006, 2011.

Moreira, A., Prats-Iraola, P., Younis, M., Krieger, G., Hajnsek, I., and Papathanassiou, K. P.: A tutorial on synthetic aperture radar, IEEE Geoscience and Remote Sensing Magazine, 1, 6–43, https://doi.org/10.1109/MGRS.2013.2248301, 2013.

Morris, K., Li, S., and Jeffries, M.: Meso- and microscale sea-ice motion in the East Siberian Sea as determined from ERS-1 SAR Data, Journal of Glaciology, 45, 370–383, https://doi.org/10.3189/s0022143000001878, 1999.

Otsu, N.: A Threshold Selection Method from Gray-Level Histograms, IEEE Transactions on System, Man, and Cybernetics, 9, 62–66, https://doi.org/10.1109/TSMC.1979.4310076, 1979.

Pratt, J. W.: Mapping bottomfast sea ice in arctic lagoons using Sentinel-1 interferometery, 2022.

Wang, Z., Liu, J., Wang, J., Wang, L., Luo, M., Wang, Z., Ni, P., and Li, H.: Resolving and analyzing landfast ice deformation by insar technology combined with sentinel-1a ascending and descending orbits data, Sensors (Switzerland), 20, 1–16, https://doi.org/10.3390/s20226561, 2020.

Winebrenner, D. P., Holt, B., and Nelson, E. D.: Observation of autumn freeze-up in the Beaufort and Chukchi Seas using the ERS 1 synthetic aperture radar, Journal of Geophysical Research: Oceans, 101, 16 401–16 419, https://doi.org/10.1029/96JC01292, 1996.

World Meteorological Organization: World Meterological Organization: WMO sea-ice nomenclature, Tech. rep., Geneva, 2014.